© 2025. Published by The Company of Biologists | Journal of Cell Science (2025) 138, jcs263483. doi:10.1242/jcs.263483

TOOLS AND RESOURCES

Focus on numbers – characterizing protein accumulation at DNA double-strand breaks

Graziana Modica[1], Joannie Roy[1], Antoine G. Godin[2,3], Hugo Wurtele[1,4,*] and Santiago Costantino[1,5,*]

ABSTRACT

Unrepaired DNA double-strand breaks can lead to cell death or genomic rearrangements. The DNA damage response (DDR) is a complex signaling cascade in which a plethora of factors act to finely tune repair pathway choice. Several DDR proteins have been shown to accumulate at sites of DNA lesions in characteristic dot-like structures known as DNA repair foci. Changes in foci brightness, commonly expressed in arbitrary intensity units, are often used as readout for DNA repair dynamics. However, due in part to technical challenges, the stoichiometry, absolute number of proteins recruited to DDR foci, and their impact on the resolution of the break remain incompletely characterized. Here, we combine spatial intensity distribution analysis (SpIDA) and a custom foci detection algorithm into an easy-to-use pipeline that, starting from confocal images, allows quantitative description of protein accumulation in DNA repair foci. Moreover, by quantifying foci based on their molecular count, SpIDA overcomes the limitations of ambiguous intensity units, enabling stoichiometric quantification between repair factors and providing a unifying means for experimental comparisons.

KEY WORDS: DNA double-strand break, DNA repair, SpIDA, 53BP1, RIF1

INTRODUCTION

The integrity of our genome is constantly challenged by threats from external and endogenous sources, including chemicals, chemotherapy drugs, reactive oxygen species and ionizing radiation (IR) (Ciccia and Elledge, 2010; Jackson and Bartek, 2009). The resulting genotoxic stress can lead to the generation of DNA double-strand breaks (DSBs), which, if left unrepaired, cause genomic instability and cell death. IR and certain chemotherapeutic compounds eliminate cancer cells by inducing high loads of DSBs. However, ensuing selection of resistant clones that are able to override DNA damage can lead to tumor relapse. Disentangling the molecular mechanisms involved in the detection and repair of DSBs is therefore crucial to develop therapeutic approaches aimed at overcoming tumor resistance to DNA-damaging treatments (Jackson and Bartek, 2009).

The DNA damage response (DDR) comprises a plethora of factors that collectively act to finely tune the repair of DNA lesions (Scully et al., 2019). Several DDR factors have been shown to accumulate at damage sites in characteristic dot-like structures called DNA repair foci (Bekker-Jensen and Mailand, 2010; Haaf et al., 1995; Maser et al., 1997). Among those, the scaffolding protein 53BP1 (also known as TP53BP1) plays a crucial role in DSB repair by steering the repairing machinery toward non-homologous end joining (NHEJ). This is achieved by favoring local recruitment of the anti-resection factors Rap1-interacting factor (RIF1) and Pax2 transactivation domain-interacting protein (PTIP, also known as PAXIP1), both requiring prior ATM-mediated phosphorylation of the N-terminal domain of 53BP1 (Boersma et al., 2015; Bothmer et al., 2010; Bouwman et al., 2010; Bunting et al., 2010; Callen et al., 2013, 2020; Chapman et al., 2013; Dev et al., 2018; Difilippantonio et al., 2008; Di Virgilio et al., 2013; Escribano-Díaz et al., 2013; Findlay et al., 2018; Ghezraoui et al., 2018; Gupta et al., 2018; Mirman et al., 2018; Munoz et al., 2007; Noordermeer et al., 2018; Setiaputra et al., 2022; Setiaputra and Durocher, 2019; Xu et al., 2015; Zimmermann et al., 2013). The recruitment of 53BP1 at DSBs depends on the recognition of pre-existing dimethylated histone H4 lysine 20 (H4K20me2) (Botuyan et al., 2006), and of *de novo* DDR-induced phosphorylation of histone H2AX (Kleiner et al., 2015) and RNF168-mediated ubiquitylation of histone H2A lysine 15 (K15) (Fradet-Turcotte et al., 2013; Gatti et al., 2012). The docking of 53BP1 on chromatin is stabilized by RIF1, whose recruitment coordinates the three-dimensional organization of 53BP1 into a spheric microdomain (Ochs et al., 2019). The accrual of 53BP1 molecules at DSBs and their inter-molecular interactions eventually cause phase separation (Kilic et al., 2019), which presumably isolates the damage site into a membrane-less compartment. Although the precise biological relevance of such phase-separated 53BP1 condensates is unclear, it has been proposed that their formation might favor DNA repair by elevating the local concentration of DDR factors around the DSB (Spegg and Altmeyer, 2021).

Fluorescence microscopy analysis of foci number and intensities are typically used as a readout to assess the dynamics of DNA repair. Intensities are expressed in arbitrary units, whose absolute values depend on imaging parameters, which hampers direct comparisons between results obtained using various experimental setups and conditions. Super-resolution microscopy has contributed to shedding light on the organization of proteins in DSB repair foci (Ochs et al., 2019; Varga et al., 2019), but the number of molecules of a DNA repair factor required to form a focus, whether and how this number is regulated, the relative stoichiometry of repair proteins on a break, as well as the interplay between factor–chromatin interactions and phase separation are important parameters that remain challenging to address using current methodologies.

[1]Maisonneuve–Rosemont Hospital Research Center, 5415, boulevard de l'Assomption, Montreal, QC H1T 2M4, Canada. [2]CERVO Brain Research Centre, Quebec Mental Health Institute, 2301, avenue d'Estimauville, Québec, QC G1E 1T2, Canada. [3]Department of Psychiatry and Neuroscience, Université Laval, Pavillon Ferdinand-Vandry, 1050 avenue de la Médecine, Québec, QC G1V 0A6, Canada. [4]Department of Medicine, Université de Montréal, 2900, boulevard Edouard-Montpetit, Montreal, QC H3T 1J4, Canada. [5]Department of Ophthalmology, University of Montreal, Pavillon Roger-Gaudry, Bureau S-700, 2900, boulevard Édouard-Montpetit, Montreal, QC H3T1J4, Canada.

*Authors for correspondence (hugo.wurtele@umontreal.ca; santiago.costantino@umontreal.ca)

G.M., 0000-0002-9229-0337; J.R., 0000-0002-7791-6629; A.G.G., 0000-0003-2417-2563; H.W., 0000-0002-5733-1711; S.C., 0000-0002-2454-2635

Handling Editor: Megan King
Received 12 August 2024; Accepted 18 April 2025

Journal of Cell Science (2025) 138, jcs263483. doi:10.1242/jcs.263483

Spatial intensity distribution analysis (SpIDA) provides information on density and oligomeric status of proteins by analyzing fluorescence intensity histograms of confocal laser scanning microscopy (CLSM) images from live or fixed samples (Godin et al., 2011; Swift et al., 2011). In CLSM images, the intensity of a pixel is the collected fluorescence intensity of all the fluorophores dwelling in the region of the sample excited by the laser focal volume, which is defined by the point spread function of the imaging system (Godin et al., 2011). Such fluorescence intensity is measured using an analog photomultiplier tube (PMT) and is a function of the PMT voltage, gain and offset, as well as the laser intensity and the scanning velocity of galvanometers.

In SpIDA, for a given region of interest in the sample, the pixel intensity histogram is fitted with a super-Poissonian distribution: all possible conformational configurations of particles in the focal volume are computed and weighted by their probability, assuming a Poisson distribution of particles in space (Barbeau et al., 2013b; Godin et al., 2011). After correcting for PMT broadening of the signal variance and for the background noise, SpIDA outputs monomer brightness (also named quantal brightness) and the density of the imaged fluorophore. SpIDA has successfully been applied to the characterization of protein oligomerization states and the dynamics of transmembrane proteins (Barbeau et al., 2013a,b; Isbilir et al., 2020; Sergeev et al., 2012a,b; Swift et al., 2011; Ward et al., 2015), the quantification of intracellular accumulation kinetics of calcein (Hamrang et al., 2014), and the diffusion rate of biofilm within microcolonies of *Streptococcus* (Buzza et al., 2023).

Here, we couple SpIDA with a custom foci segmentation software to investigate protein recruitment at DNA DSBs. We describe the performance of a pipeline for detection and quantification of the number of molecules per focus for a given protein applied to both direct [i.e. a protein tagged with monomeric EGFP (mEGFP)] and indirect fluorescence (antibody labeling). We show the applicability of the approach to simultaneously analyze foci kinetics of two proteins, 53BP1 and its interactor RIF1, and to describe their stoichiometric relationship in response to DNA damage.

RESULTS

Tailoring SpIDA to quantify molecules at DNA repair foci

We sought to investigate the dynamics of protein recruitment at DSBs using a high-content approach based on the intensity of foci labeled with a fluorescent reporter. We applied SpIDA to determine the monomer brightness (MB) of the fluorophore used (Fig. 1A–C) and then calculated the number of molecules per focus based on their intensities (Fig. 1D,E). We segmented the repair foci from the nuclei of cells and estimated the number of molecules per focus as the ratio between the integral of their pixel intensities and the MB of the fluorescent probe, which can either be a fluorescent protein or an antibody-conjugated dye (Fig. 1B,E). The quantification of MB of the reporter via SpIDA requires a confocal image where monomers are homogeneously distributed in the region scanned by the laser. Furthermore, since the quantum yield of fluorophores often depends on the local biochemical environment, the MB must be calculated inside the nucleus to allow comparison with nuclear proteins. For this, we engineered U2OS osteosarcoma cells to stably express mEGFP fused at the C terminus with the HA tag (Fig. 1B; Fig. S1A). This allowed us to (1) calculate the average brightness of one molecule of GFP and (2) to calculate the average brightness of one fluorescent antibody complex, by performing immunofluorescence with a monoclonal antibody against HA, followed by a secondary antibody conjugated with Alexa-Fluor 647.

The MB was measured in each experiment, as it depends on the specific acquisition settings [laser power, PMT gain (Fig. S1G,H), pinhole size and pixel dwell time], which are adjusted considering biological and technical variables such as expression levels or the efficacy of immunofluorescence labeling. For every measurement, the same parameters used for imaging DNA repair foci were replicated to probe the MB of the fluorescent reporter. We used DAPI staining to segment nuclei and SpIDA to analyze the histograms of the fluorescence of nuclear pixels (Fig. 1C, top). Intensity histograms were fitted with super-Poissonian distributions, and only ones with a goodness-of-fit less than 0.15 were considered for analysis (Fig. 1C, middle; Fig. S1C). Furthermore, to avoid concentration gradients and heterogeneous distributions of protein (Barbeau et al., 2013a), which can yield artifacts, we applied a median filter to each nucleus and only preserved cells displaying a low standard deviation of the intensity values (s.d.<0.035; Fig. 1C, bottom; Fig. S1B,C). Finally, the MB of the cell ensemble was obtained as the mean of the MB values of individual cells (Fig. S1D).

We chose to test our SpIDA-based pipeline by characterizing formation of 53BP1 foci in response to DNA damage induced by the radiomimetic drug Zeocin (Fig. 1D). To avoid artefacts due to abnormal expression levels, we used CRISPR-Cas9 to generate a knock-in U2OS cell line in which the coding sequence for mEGFP was inserted in-frame at the C terminus of the endogenous *53BP1* locus (Kilic et al., 2019). The majority of our analysis was performed using a homozygous clone (53BP1–mEGFP$^{+/+}$; Fig. S1E,F), whereas we used a quantitative PCR (qPCR)-validated heterozygous clone in which half of the 53BP1 alleles were tagged with mEGFP (53BP1–mEGFP$^{+/-}$; Fig. S1E,F) as a control (see Fig. 2; Fig. S3A–C, Fig. S4A–C). We next induced DNA damage by treating 53BP1–mEGFP cells with Zeocin, followed by segmentation of 53BP1 foci in microscopy images using a previously published algorithm (Bélanger et al., 2016; Binan et al., 2019) (Fig. 1D). The segmentation was based either on mEGFP signal or staining with an anti-53BP1 monoclonal antibody coupled with the same fluorophore-conjugated secondary antibody used to calculate the MB, that is, either Alexa-Fluor 647 or Alexa-Fluor 546 fluorophore (Fig. 1E). For each fluorophore we calculated the number of foci per cell (Fig. 1F; Fig. S2A,B), the brightness of each focus, obtained as the sum of intensity of all the pixels in a given focus (Fig. 1G; Fig. S2C,D), and converted the brightness in molecules per focus via MB normalization (Fig. 1H; Fig. S2E,F).

Treating the cells with Zeocin induced a significant increase in the number of foci per cell compared to that of the untreated control (Fig. 1F; Fig. S2A,B). In cells not exposed to exogenous stress, we observed the presence of large 53BP1 foci-like structures, which have previously been termed 53BP1 nuclear bodies (Bekker-Jensen et al., 2005; Harrigan et al., 2011; Lukas et al., 2011). Such structures are typically observed in G0/G1-phase cells and are mostly associated with under-replicated DNA (UR-DNA) inherited by the daughter cells from the previous cell cycle (Lukas et al., 2011). 53BP1 nuclear body formation in G1 segregates such regions in defined nuclear compartments, protecting UR-DNA from further damage and timing their repair to late S phase (Spies et al., 2019). 53BP1 nuclear bodies have been observed in a variety of cell types and are typically larger and brighter than DNA damage-induced foci (Lukas et al., 2011). Accordingly, when calculated using mEGFP, in untreated cells, we observed few nuclear bodies, each containing a higher number of 53BP1 molecules per focus compared to those in Zeocin-treated cells [Fig. 1H; Fig. S2G; 7512±1383 and 4625±1025 molecules per focus (all values are mean±s.d.) in untreated cells and Zeocin-treated cells, respectively]. When analyzed via immunofluorescence with either

Journal of Cell Science (2025) 138, jcs263483. doi:10.1242/jcs.263483

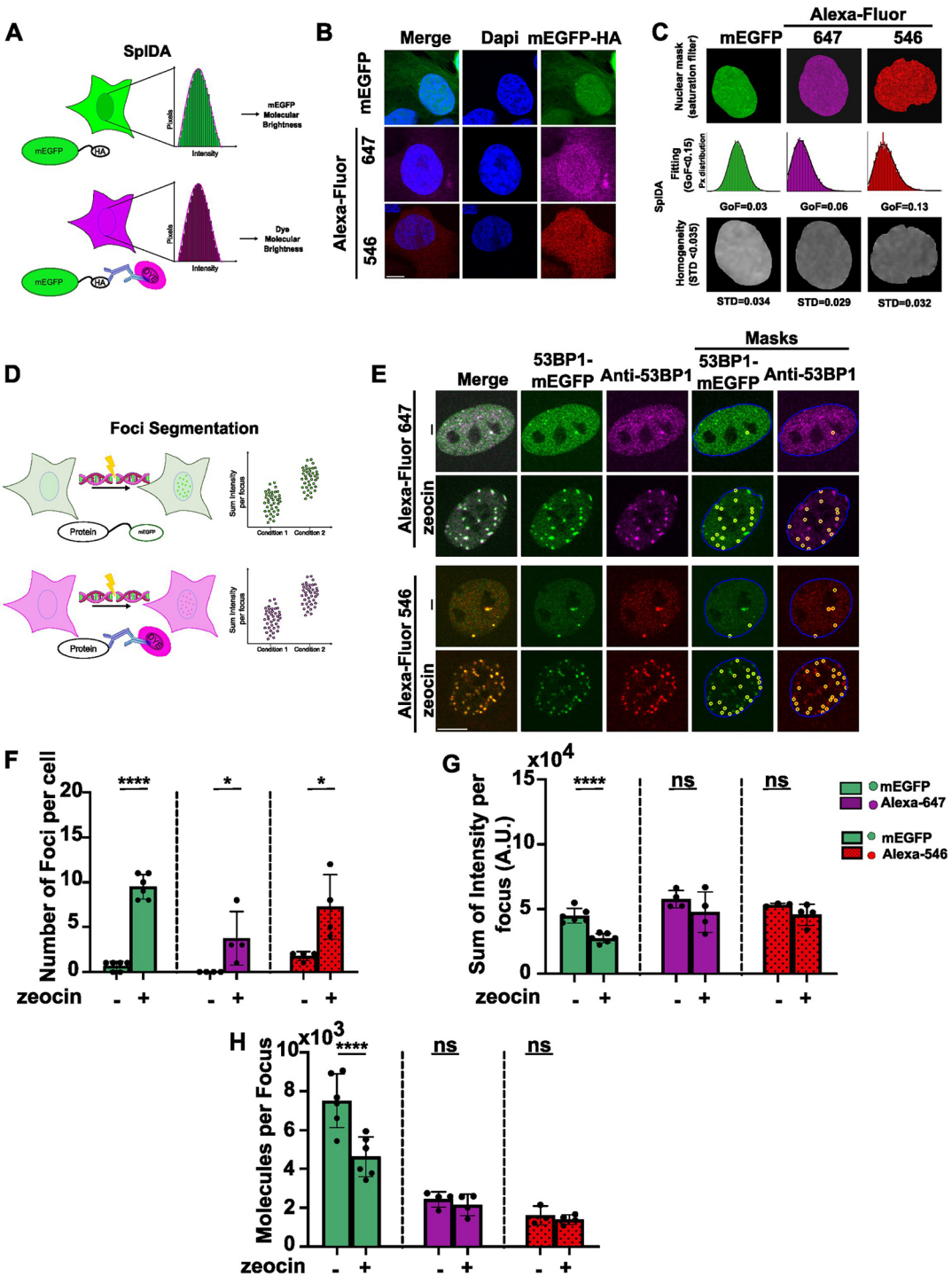

Fig. 1. SpIDA allows the conversion of arbitrary intensity units into an absolute number of molecules. (A) Workflow for MB calculation using SpIDA. (B) U2OS cells stably expressing mEGFP–HA were fixed, and immunofluorescence was performed against HA. Signal was revealed using either Alexa-Fluor 647 (middle) or Alexa-Fluor 546 (bottom). DAPI (blue) was used as nuclear marker. (C) Image processing workflow, illustrated using cells as shown in B. Nuclei were segmented using the DAPI channel, and images were filtered to eliminate cells with saturated pixels (top row). SpIDA was performed on pixel intensity distributions; representative histograms with goodness-of-fit (GoF) below the cut-off threshold of 0.15, as well as the relative fitted curves, are shown for each analyzed channel (middle row). Homogeneity was assessed via applying a median filter and selecting for nuclei with a pixel intensity standard deviation (STD) of less than 0.035. Representative output and STD values are shown for each channel. (D) Scheme of DNA repair foci induction and segmentation. (E) U2OS cells expressing 53BP1 fused at the endogenous locus with mEGFP (53BP1–mEGFP$^{+/+}$) were treated or not for 1 h with 500 µg/ml Zeocin as indicated, followed by medium replacement, 1 h incubation, and fixation in 4% PFA. Immunofluorescence with monoclonal antibody against 53BP1 was performed using a secondary antibody conjugated with Alexa-Fluor 647 or Alexa-Fluor 546, as indicated. For each channel, an example of foci segmentation is shown (fourth and fifth columns). (F–H) Representative distribution of the number of foci per cell (F), sum of intensity per focus (G) and number of molecules per focus (H) for n>200 cells per condition for each replicate of experiments as shown in E. Data are plotted as mean±s.d. Each data point represents the median of n>200 cells per condition per experiment, for each of $n\geq3$ replicates. A.U., arbitrary unit. *$P\leq0.05$; ****$P\leq0.0001$; ns, not significant (unpaired, two-tailed Student's t-test). Scale bars: 10 µm.

Journal of Cell Science (2025) 138, jcs263483. doi:10.1242/jcs.263483

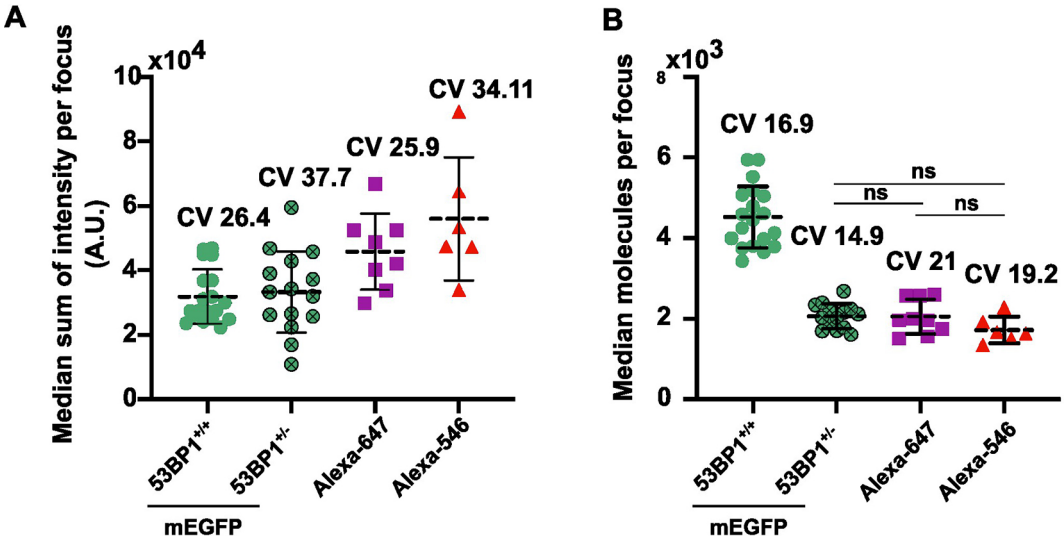

Fig. 2. SpIDA reduces inter-experimental variability. (A,B) Comparison of the median values of sum of intensity per focus (A) and number of molecules per focus (B) in 53BP1–mEGFP$^{+/+}$ and 53BP1–mEGFP$^{+/-}$ cells treated with 500 µg/ml Zeocin, calculated using mEGFP, Alexa-Fluor 647 or Alexa-Fluor 546, as indicated. Alexa-Fluor data are pooled from both genotypes. Each dot represents the median value from one replicate, n>200 cells were sampled per replicate. n≥5 replicates. Dashed line marks mean; error bars show s.d. A.U., arbitrary unit; CV, coefficient of variation. ns, not significant (unpaired, two-tailed Student's t-test).

Alexa-Fluor 647 or Alexa-Fluor 546, results were consistent both in terms of intensity and number of molecules per focus between untreated and treated samples (Fig. 1G,H; Fig. S2C–F). However, we found that the number of molecules per foci was ∼2-fold lower when using immunofluorescence than was observed when using mEGFP (Fig. 1H). We believe that this difference is likely due to limited epitope accessibility for the antibody in foci (see below and Discussion).

When expressing foci brightness as arbitrary intensity units, the differences in image acquisition settings and in the quantum yield values of specific fluorophores (Cranfill et al., 2016; https://www.aatbio.com/resources/quantum-yield/alexa_fluor_546, retrieved 16 April 2024) prohibit meaningful inter-channel comparisons. However, when SpIDA is applied, normalization with MB values allows compensation for such variables, enabling comparison between channels. Indeed, we observed that the number of molecules per focus calculated via antibody labeling was comparable for the two secondary antibodies used (Fig. 1H; Fig. S2E–G), Finally, the number of molecules per focus did not change when calculated using immunofluorescence labeling of U2OS cells in which 53BP1 was not tagged with mEGFP (Fig. S2H,I), suggesting that the presence of the tag does not significantly affect 53BP1 foci formation.

To test whether the lower number of molecules we observed in immunofluorescence compared to mEGFP tagging is imputable to antibody availability, we performed antibody titration tests. Using 1:400, 1:800 and 1:1600 antibody dilutions with Zeocin-treated cells resulted in 1773±1040, 1564±938 and 1428±876 calculated 53BP1 molecules per focus (Fig. S2J). Thus, the difference in the number of molecules is only 10% higher when comparing the 1:400 and 1:800 dilutions, suggesting that antibody availability during the labeling procedure is not limiting. We also performed the same experiment on the 53BP1–mEGFP heterozygous clone (53BP1–mEGFP$^{+/-}$) (Fig. S1E,F, Fig. S3A–C). Applying SpIDA, we calculated 2197±490 molecules per focus in the mEGFP channel (Fig. S3B,C), which is ∼2-fold lower than values obtained for the homozygous clone (Fig. 1H). Moreover, we calculated 1741±796 and 1924±319 molecules per focus using Alexa-Fluor 647 (Fig. S3B) and Alexa-Fluor 546 (Fig. S3C) immunofluorescence, respectively, which is similar to the values obtained in the homozygous clone (Fig. S2G).

To assess the consistency of SpIDA, we calculated the coefficient of variation (s.d./mean) among the median sum of intensity per focus and the number of 53BP1 molecules per focus in cells treated with 500 µg/ml Zeocin across all the experiments performed, comparing the mEGFP, Alexa-Fluor 647 and Alexa-Fluor 546 results, including data collected from the 53BP1–mEGFP$^{+/-}$ clone. Importantly, these data originate from samples imaged on different confocal systems and with different acquisition parameters. We found that the absolute value of the sum of intensity per experiment was highly variable both intra- and inter-dataset, with a coefficient of variation spanning from 25.9% to 37.7% for the Alexa-Fluor 647 and mEGFP channels, respectively (Fig. 2A). However, when expressed as the number of molecules per focus, intra- and inter-group differences were not significant, with a coefficient of variation ranging from 14.9% to 21.0% for the mEGFP and Alexa-Fluor 647 channels, respectively (Fig. 2B). These data demonstrate that expressing brightness as a number of molecules rather than arbitrary intensity units not only improves reproducibility but also enables comparisons between different fluorophores and imaging systems.

SpIDA reveals the stoichiometry of RIF1 and 53BP1 at DDR foci

Repair pathway choice for a given DNA break is the result of the contribution of the cell cycle phase, the availability of repairing factors, as well as the characteristics of the surrounding chromatin (Scully et al., 2019). Several proteins are simultaneously recruited to DNA repair foci, and their mutual stoichiometries are thought to be important to coordinate the resolution of the damage. RIF1 is recruited at DSBs via interaction with phosphorylated 53BP1 and blocks the recruitment of pro-resection factors, directing DSB repair toward NHEJ (Chapman et al., 2013; Ochs et al., 2019; Setiaputra et al., 2022). To quantitatively characterize the interplay between these proteins at DSBs, we simultaneously examined focus formation for 53BP1–mEGFP and, leveraging the antibody-based

Journal of Cell Science (2025) 138, jcs263483. doi:10.1242/jcs.263483

version of SpIDA, RIF1. We analyzed the extent to which the number of molecules per focus changes when the availability of 53BP1 is reduced and evaluated whether this quantitatively affects RIF1 foci. 53BP1 expression was downregulated via small interfering RNA (siRNA; Fig. 3A–C), which led to a ∼3-fold decrease in the total number of 53BP1 molecules compared to that in untreated cells (Fig. 3B,C; Fig. S3D). Reduced availability of 53BP1 hampered the formation of Zeocin-induced foci (Fig. 3D; Fig. S3F) and led to the accumulation of 1590±339 and 1498±266 molecules per focus (mean±s.d.) in cells treated with 1 nM or 5 nM of 53BP1-targeted siRNA, respectively (Fig. 3E,F; Fig. S3H). This represents a ∼3-fold decrease compared to non-targeting siRNA-treated cells (4125±658 molecules per focus; Fig. 3E,F). The reduced number of molecules per focus in 53BP1-depleted cells does not indicate that the detection limit of the imaging system was reached; indeed, when the same experiment was performed using the 53BP1–mEGFP$^{+/-}$ clone (Fig. S4A–C), we counted 2300±300, 1000±300 and 800±200 molecules per focus in cells treated with non-targeting siRNA, or with 1 nM or 5 nM of 53BP1-targeted siRNA, respectively (Fig. S4C), indicating that our system is capable of detecting foci containing only ∼800 53BP1–mEGFP molecules.

In the case of RIF1, Zeocin treatment led to the formation of foci containing a median value of 2080±365 molecules per focus. This value remained consistent when a different fluorophore was used for detection (Fig. S4D,E) and was not limited by antibody availability (Fig. S4F). Upon siRNA-mediated depletion of 53BP1, we observed a decrease in the number of RIF1 foci per cell (Fig. 3D; Fig. S3G). 53BP1 depletion did not affect the total number of RIF1 molecules (Fig. 3C; Fig. S3E), but we observed a modest decrease in the number of RIF1 molecules per focus (Fig. 3E,F; Fig. S3I) that did not reach statistical significance [1876±435, 1477±330 and 1650 ±276 in cells treated with non-targeting siRNA, or with 1 nM or 5 nM of 53BP1-targeted siRNA, respectively]. Moreover, in cells treated with non-targeting siRNA, ∼11% of 53BP1 foci per cell were devoid of RIF1 on average, whereas all remaining 53BP1 foci colocalized with RIF1 foci in cells treated with 53BP1 siRNA. Conversely, almost all RIF1 foci colocalized with 53BP1 foci in the presence or absence of 53BP1 siRNA, as expected (Fig. S4G,H).

ATM inhibition impacts RIF1 accumulation at DSBs

RIF1 recruitment at DSBs depends on the interaction with ATM-mediated phosphorylation of the N terminus of 53BP1 (Setiaputra et al., 2022). To test whether SpIDA could detect changes in RIF1 accumulation at repair foci, we treated cells with the ATM inhibitor KU55933 prior to Zeocin exposure (Fig. 4A). The inhibitor did not impact the total amount of either 53BP1 or RIF1 per cell (Fig. 4B; Fig. S5A,D). In accord with previously published work (Bakr et al., 2016; Becker et al., 2014; Harding et al., 2011; Meador et al., 2022), ATM inhibition did not completely abolish 53BP1 accumulation at DSBs but caused a ∼50% decrease in the number of 53BP1 foci, a trend that did not, however, reach statistical significance (Fig. 4C; Fig. S5B). In contrast, RIF1 focus formation was significantly compromised when cells were treated with the highest ATM inhibitor dose, as previously reported (Bakr et al., 2016) (Fig. 4C; Fig. S5E). Despite the decrease in the quantity of foci per cell, the number of 53BP1 molecules per focus in KU55933-treated cells did not change significantly compared to cells that were treated only with Zeocin (Fig. 4C–E; Fig. S5C). Since ATM inhibition strongly impacts RIF1 ability to form detectable foci, we segmented 53BP1 foci and calculated the number of molecules of RIF1 in these nuclear regions. As expected, KU55933 treatment induced a significant reduction in the number of RIF1 molecules at 53BP1 foci (Fig. 4C–E; Fig. S5F).

Impact of NuMA-dependent reduction in 53BP1 availability on repair foci

In the nucleoplasm, the reservoir of 53BP1 that is available to form foci is regulated by Lamin B1 (Etourneaud et al., 2021) and NuMA (also known as NuMA1) (Salvador Moreno et al., 2019). Modulation of NuMA expression has previously been shown to influence the number and intensity of 53BP1 foci, without altering the total cellular amount of the protein (Salvador Moreno et al., 2019). We applied SpIDA to calculate the number of molecules per focus in cells treated with Zeocin with or without transient overexpression of mCherry–NuMA (Fig. 5A,B). Consistent with published data (Salvador Moreno et al., 2019), elevated expression of NuMA reduced the number of Zeocin-induced 53BP1 foci (Fig. 5C; Fig. S5G) as well as the number of 53BP1 molecules per focus (Fig. 5D,E; Fig. S5H). As expected, increased expression of NuMA did not reduce the total amount of 53BP1 (Salvador Moreno et al., 2019) (Fig. 5B,F; Fig. S5I).

Modulation of 53BP1 foci formation in response to increasing DSB load

The number of 53BP1 foci per cell has been shown to peak at 4 Gy IR treatment and to plateau between 4 Gy and 8 Gy IR treatment (Ochs et al., 2016), due to TRIP12- and UBR5-mediated repression of the histone ubiquitylase RNF168 (Gudjonsson et al., 2012), a protein required for 53BP1 accumulation at DSBs. Challenging cells with increasing doses of Zeocin induced a similar behavior with regards to 53BP1 foci formation (Figs 6A,C and 7A,B). Upon Zeocin treatment, the number of foci per cells plateaued between 500 µg/ml and 1000 µg/ml (14±0.6 and 14±2.6, respectively; mean ±s.d.) and decreased at 5000 µg/ml (2±1.7) (Fig. 6A,C; Fig. S6A). We also observed that the fraction of 53BP1 recruited to foci peaked between 500 µg/ml and 1000 µg/ml (38±7% and 36.5±2%; mean±s.d.) and decreased at 5000 µg/ml (Fig. 6B), suggesting that a significant fraction of the nucleoplasmic pool of 53BP1 is not available to accumulate at DSB repair foci. Concordantly, the number of 53BP1 molecules per focus decreased with increasing Zeocin doses to reach a median value of 4687±603, 3957±726 and 3854±445 molecules per focus (mean±s.d.) at 500 µg/ml, 1000 µg/ml and 5000 µg/ml (Fig. 6D; Fig. S6C,H). In accordance with published work (Gudjonsson et al., 2012; Ochs et al., 2016), the reduction in the fraction of 53BP1 recruited to foci was not due to diminished 53BP1 expression, since the total protein amount did not significantly change among conditions used in this experimental setup (Fig. 6E; Fig. S6E,G). The number of RIF1 foci per cell mirrored the behavior of 53BP1, decreasing at higher doses of Zeocin (Fig. 6A,C; Fig. S6B). However, in contrast to 53BP1, the number of molecules per focus did not significantly change with increasing Zeocin concentration (Fig. 6D; Fig. S6D,H). The number of 53BP1 molecules in RIF1-colocalizing foci versus non-colocalizing foci slightly increased at 10 µg/ml of Zeocin but did not change significantly at higher Zeocin concentration (Fig. 6F), suggesting that RIF1 recruitment might impact the structure and/or organization of 53BP1 foci without significantly altering the number of molecules of this protein. This is consistent with published observations indicating that RIF1 depletion does not impact the brightness of 53BP1 foci (Ochs et al., 2019).

We observed comparable behavior when cells were exposed to increasing IR doses: the number of both 53BP1 and RIF1 foci increased following IR treatments of up to 4 Gy and started to

Journal of Cell Science (2025) 138, jcs263483. doi:10.1242/jcs.263483

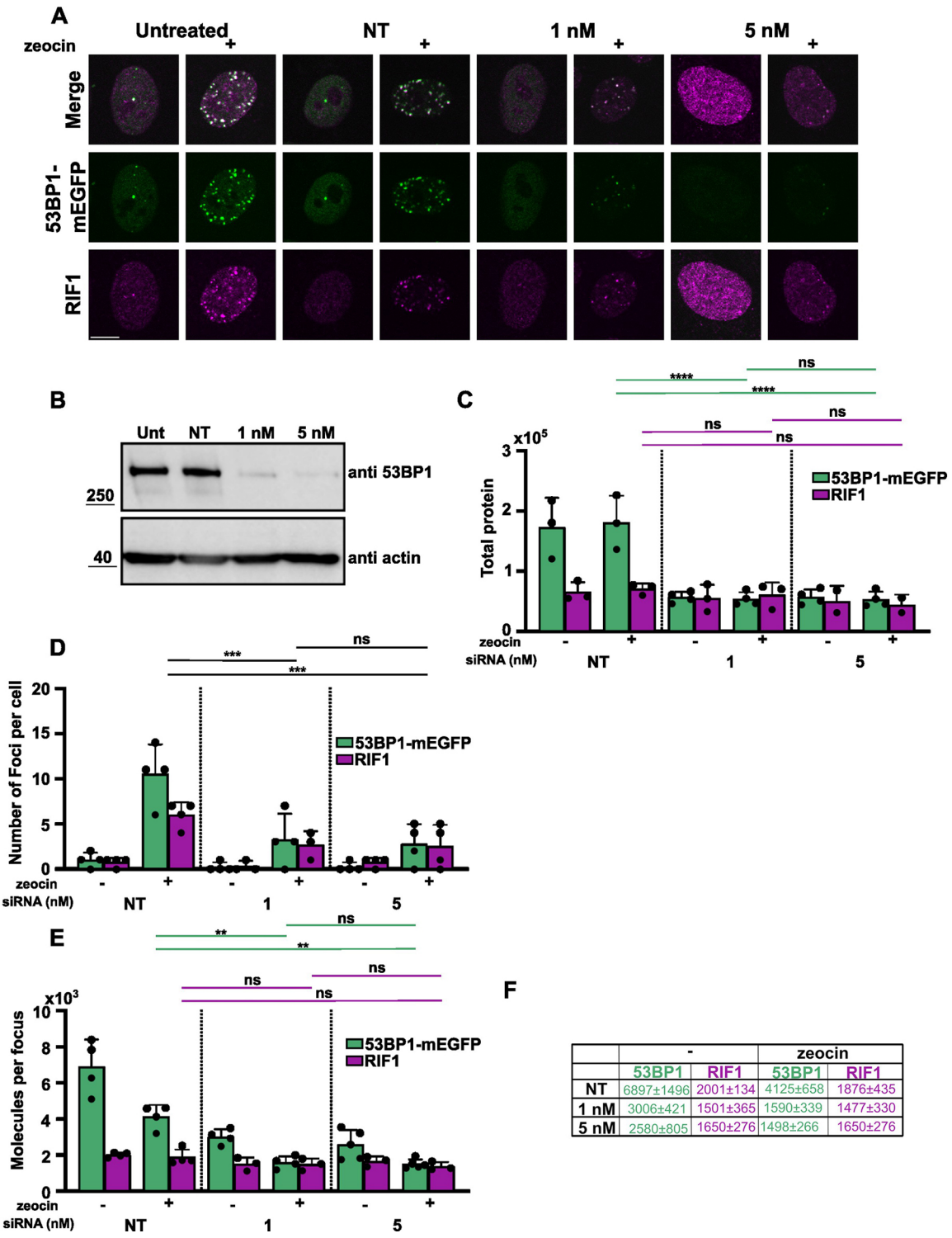

	-		zeocin	
	53BP1	RIF1	53BP1	RIF1
NT	6897±1496	2001±134	4125±658	1876±435
1 nM	3006±421	1501±365	1590±339	1477±330
5 nM	2580±805	1650±276	1498±266	1650±276

Fig. 3. Stoichiometry of 53BP1 and RIF1 at repair foci. (A) 53BP1 focus formation upon siRNA-mediated downregulation. 53BP1–mEGFP$^{+/+}$ U2OS cells were either not treated with siRNA (untreated) or were transfected with non-targeting siRNA (NT) or the indicated concentration of siRNA against 53BP1. At 48 h after transfection, cells were treated with 500 µg/ml Zeocin as indicated. Cells were fixed, and immunofluorescence was performed using an anti-RIF1 rabbit recombinant monoclonal antibody. Samples were imaged using a confocal system and analyzed using our automated foci detection algorithm. Scale bar: 10 µm. (B) Immunoblotting validation of 53BP1 knockdown. Lysates from 53BP1–mEGFP$^{+/+}$ cells, either untreated (Unt) or treated with siRNA as described in A, were loaded on a 6% or 12% gel for SDS-PAGE before immunoblotting with anti-53BP1 or anti-actin antibodies, respectively. Molecular masses are indicated in kDa. Blots shown are representative of three experiments. (C) 53BP1–mEGFP (green) and RIF1 (magenta) total molecules at the focal plane for experiments as shown in A. (D) Number of 53BP1 (green) and RIF1 (magenta) foci per cell for experiments as shown in A. (E) Average molecules per focus for experiments as shown in A. Data in C–E are plotted as mean±s.d. Dots represent the median values for each of $n\geq3$ independent experiments, where $n>200$ cells per condition were sampled in each replicate. Statistical comparisons for Zeocin-treated cells in D refer to the 53BP1–mEGFP distributions, those in C and E are color-coded for 53BP1–mEGFP and RIF1. ns, not significant; $^{**}P\leq0.01$; $^{***}P\leq0.001$; $^{****}P\leq0.0001$ (one-way ANOVA with Tukey's post-hoc test). (F) Molecules per focus of 53BP1–mEGFP and RIF1 in mock- or Zeocin-treated cells with the indicated siRNA treatment. Data are mean±s.d.

Journal of Cell Science (2025) 138, jcs263483. doi:10.1242/jcs.263483

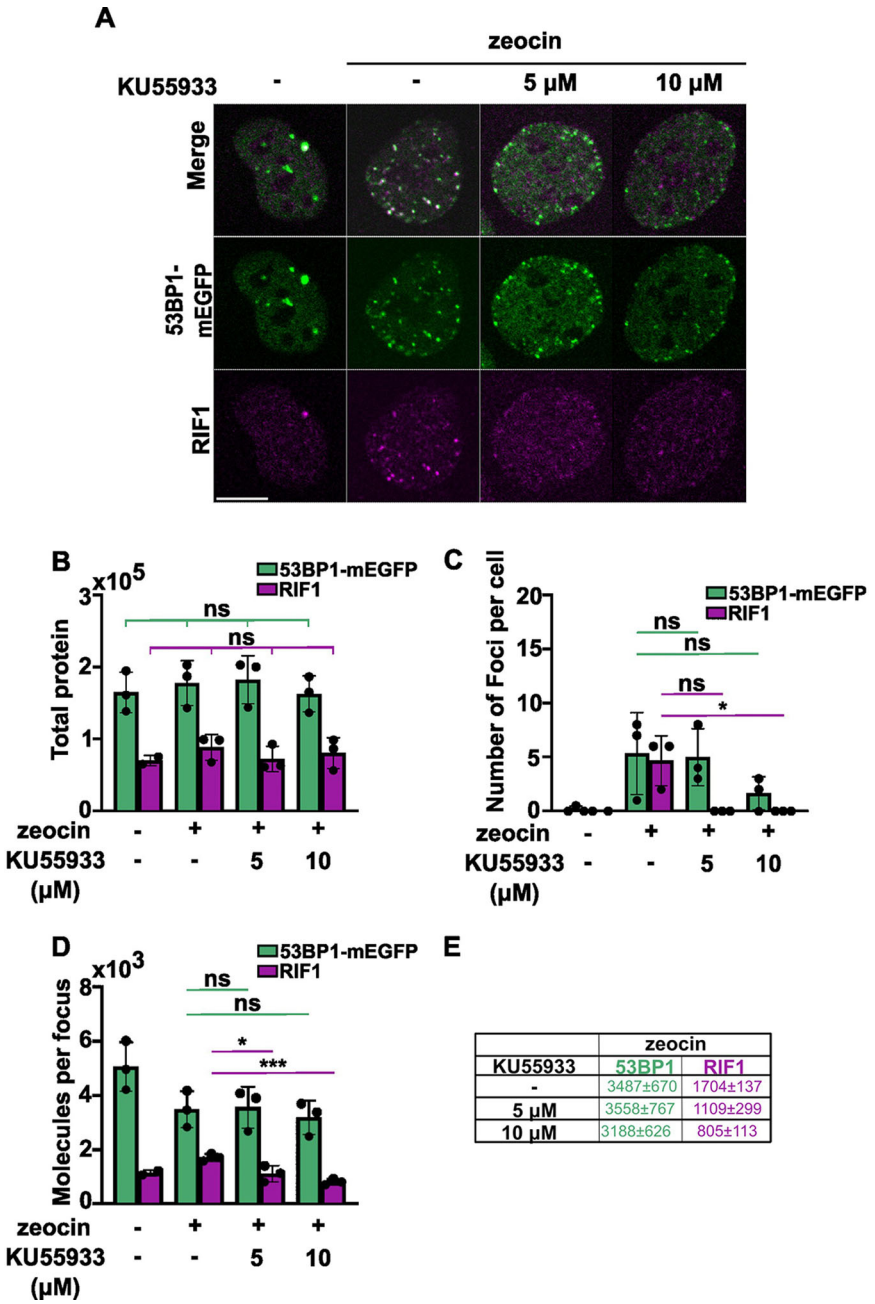

	zeocin	
KU55933	53BP1	RIF1
-	3487±670	1704±137
5 µM	3558±767	1109±299
10 µM	3188±626	805±113

Fig. 4. SpIDA detects reduced RIF1 recruitment to repair foci upon ATM inhibition. (A) 53BP1 and RIF1 focus formation in cells treated with ATM inhibitor and exposed to Zeocin. 53BP1–mEGFP$^{+/+}$ cells were treated for 30 min with 5 µM or 10 µM of KU55933 as indicated, followed by 500 µg/ml Zeocin treatment for 1 h, medium replacement, 1 h recovery and fixation in 4% PFA. Where indicated, the inhibitor was kept in the medium during the Zeocin treatment and recovery. Immunofluorescence was performed using an anti-RIF1 rabbit recombinant monoclonal antibody. Samples were imaged using a confocal system and analyzed using our automated foci detection algorithm. Scale bar: 10 µm. (B–D) 53BP1–mEGFP (green bars) and RIF1 (magenta bars) total molecules per cell (B), number of foci per cell (C) and number of molecules per focus (D). Data are plotted as mean ±s.d. Dots represent the median values for each of $n \geq 3$ independent experiments, where $n > 200$ cells per condition were sampled in each replicate. All combinations of groups were tested in a pairwise manner using *t*-tests. ns, not significant; $^{*}P \leq 0.05$; $^{***}P \leq 0.001$ (unpaired, two-tailed Student's *t*-test). (E) Average molecules per focus of 53BP1–mEGFP and RIF1 for the indicated conditions. Data are mean±s.d.

decrease at higher doses (Fig. 7A,B; Fig. S7A,B). Consistently with what we observed upon Zeocin treatment, the total amount of protein did not change for both factors (Fig. 7C; Fig. S7C,D); the number of molecules of 53BP1 per focus decreased with increasing IR doses to reach a median value of 4848±971, 3972±669 and 3687±761 molecules per focus at 2 Gy, 4 Gy, and 12 Gy, respectively (Fig. 7D; Fig. S7E,G,H), whereas the amount of RIF1 did not vary significantly with increased DSB load (Fig. 7D; Fig. S7F–H).

DISCUSSION

The use of SpIDA to calculate the number of molecules inside and/or outside foci allows quantitative analysis of protein abundance, stoichiometries and recruitment to sites of DNA damage, which are expected to influence DSB repair focus formation and resolution. In a confocal imaging system, the collected intensity of a pixel depends not only on the fluorophore quantum yield, but also on the relative contribution of laser power, PMT voltage and gain, pinhole size and pixel dwell time. Thus, even without accounting for the intrinsic variation of biological systems and sample preparation, the imaging degrees of freedom per se heavily impact data reproducibility between laboratories. We demonstrate that calculating the brightness of a single molecule of fluorophore in a given imaging configuration and normalizing the acquired data by such monomeric brightness significantly reduces the variance between replicates. Moreover, by describing a focus in terms of number of molecules instead of arbitrary intensity units, SpIDA enables robust inter-experiment comparisons.

While super-resolution microscopy approaches allow unprecedented characterization of the organization of proteins within foci, including 53BP1 and phosphorylated histone H2AX (Ochs et al., 2019; Varga et al., 2019), the need for expensive equipment, user expertise, complex sample preparation and precise

Journal of Cell Science (2025) 138, jcs263483. doi:10.1242/jcs.263483

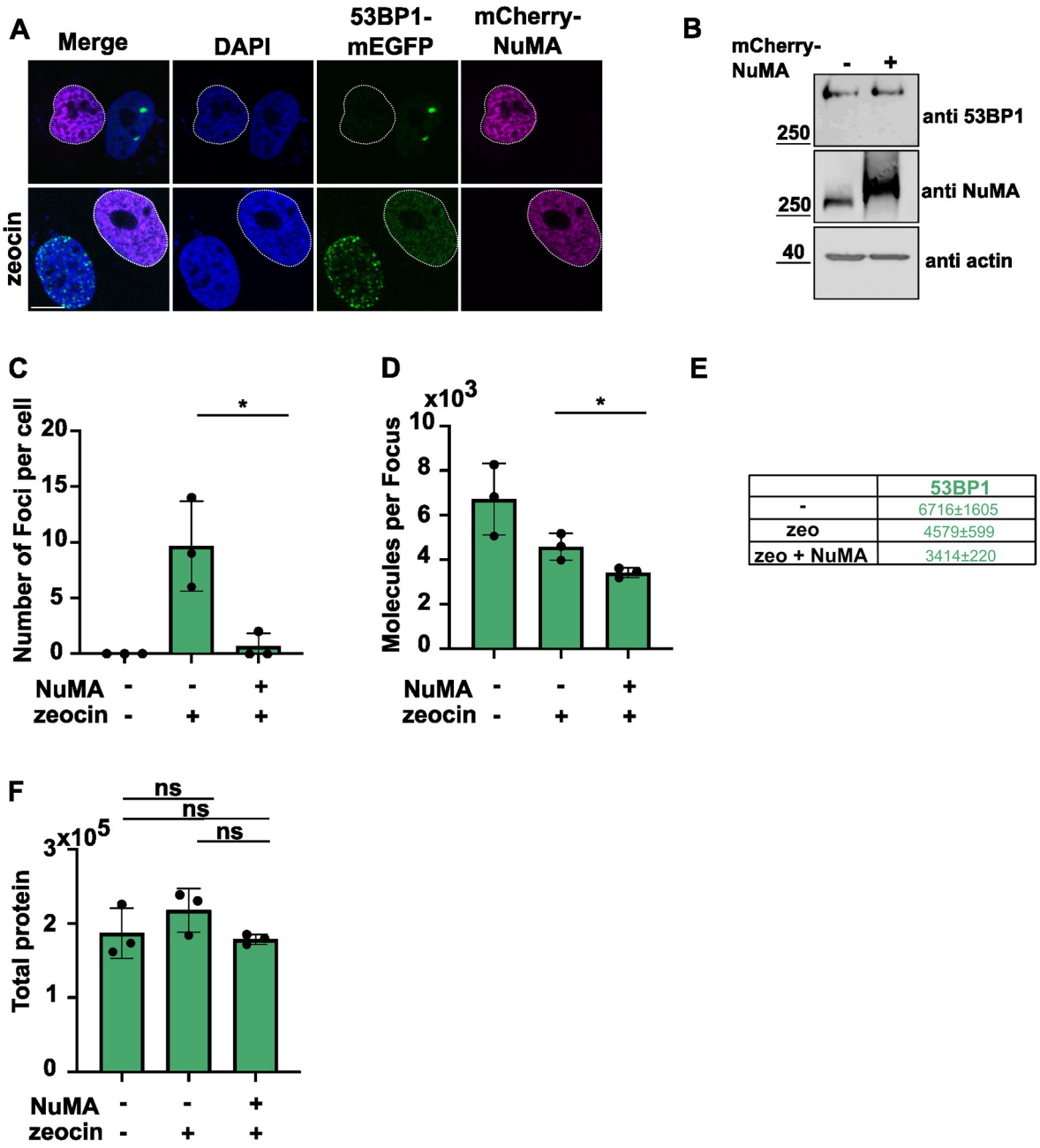

Fig. 5. NuMA overexpression reduces the number of 53BP1 molecules at repair foci. (A) 53BP1 foci formation upon NuMA overexpression. 53BP1–mEGFP$^{+/+}$ cells were transfected with mCherry–NuMA (dotted outlines indicate transfected nuclei) and challenged with 500 µg/ml of Zeocin as indicated, fixed and imaged. Scale bar: 10 µm. (B) Immunoblotting validation of mCherry–NuMA overexpression. Lysates from 53BP1–mEGFP$^{+/+}$ cells transfected or not with mCherry–NuMA were loaded for SDS-PAGE on a 6% (53BP1, NuMA) or 12% (actin) gel before immunoblotting with anti-53BP1, anti-NuMA or anti-actin antibodies. Molecular masses are indicated in kDa. Blots shown are representative of three experiments. (C–F) Number of foci per cell (C), number of molecules per focus (D), average number of molecules per focus (E) and total amount of 53BP1 per cell expressed as number of molecules per cell (F) for experiments as shown in A. In C, D and F, data are plotted as mean±s.d. Black dots indicate the median values for each of $n \geq 3$ replicates, with $n \geq 100$ cells per condition each replicate. Data in E are mean±s.d. *$P \leq 0.05$; ns, not significant (unpaired, two-tailed Student's *t*-test).

fluorophore selection has hampered widespread adoption of these methodologies (Lambert and Waters, 2017). In contrast, SpIDA only requires confocal imaging, can operate on fixed samples, is less sensitive to photodamage and allows repeated measurements, which simplifies image acquisition in the context of multiple replicate experiments (Barbeau et al., 2013a; Godin et al., 2011).

Resolving protein abundance and stoichiometry in foci has previously been performed in an overexpression system, using viral-like particles (VLP) assembled with yellow fluorescent protein (YFP)-tagged HIV-1 GAG protein as *in situ* standards. Titration curves make it possible to derive the number of molecules per focus of the protein of interest labeled with the same fluorescent protein as the one used to assemble the VLP (Mok and Henderson, 2012a,b). Compared to SpIDA, the VLP-standard approach is limited to the use of fluorescent fusion proteins and therefore does not allow the flexibility of using antibodies, does not take into consideration the effect of the subcellular compartment on fluorescence emission of the reporter protein and is technically more laborious.

Journal of Cell Science (2025) 138, jcs263483. doi:10.1242/jcs.263483

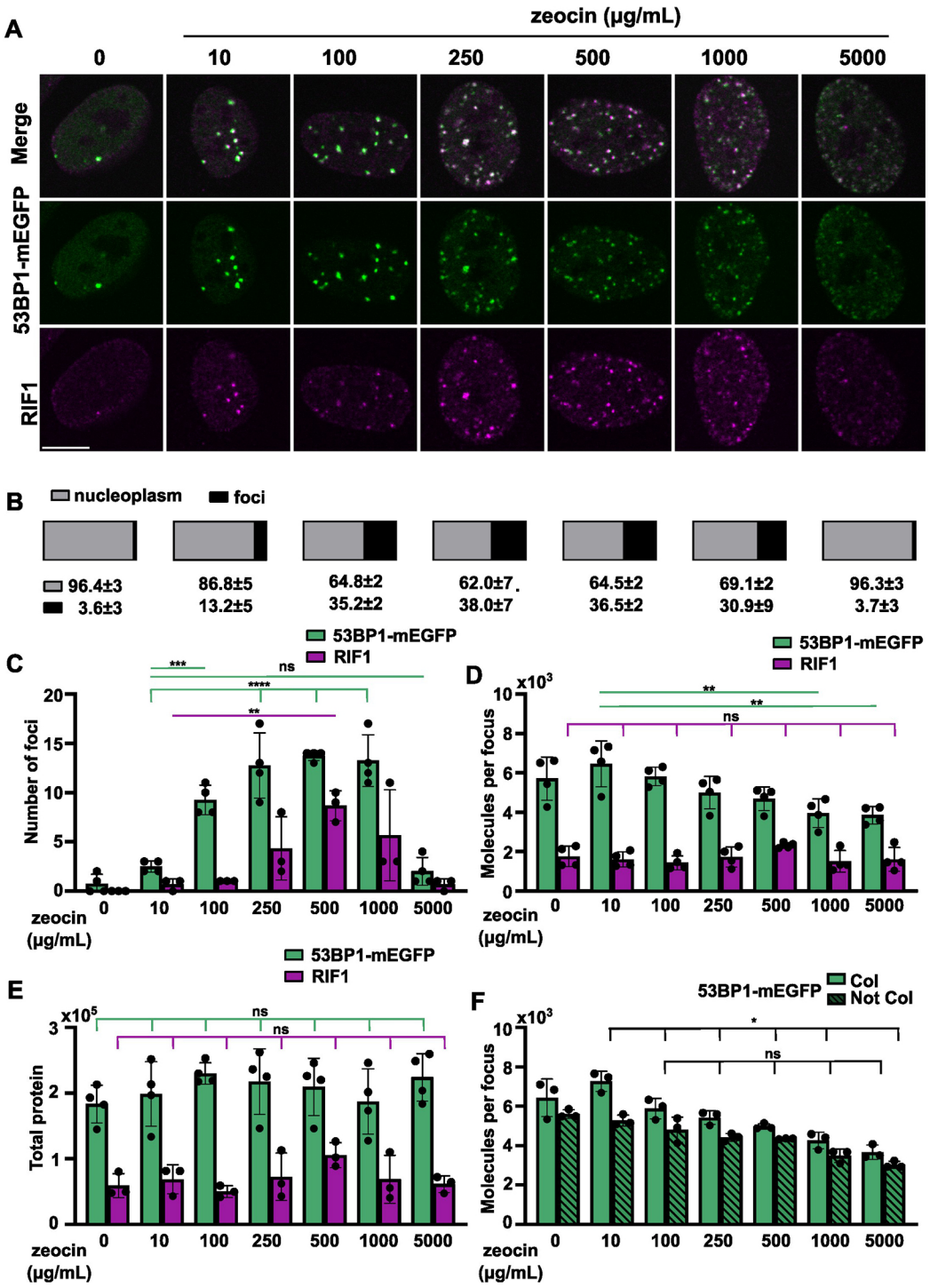

Fig. 6. 53BP1 and RIF1 show different accumulation dynamics at repair foci upon treatment with increasing Zeocin concentrations. (A) Response of 53BP1 and RIF1 foci to increasing DNA damage load. 53BP1–mEGFP$^{+/+}$ cells were treated with the indicated concentration of Zeocin for 1 h , followed by medium replacement, 1 h incubation and fixation in 4% PFA. Immunofluorescence was performed using an anti-RIF1 rabbit recombinant monoclonal antibody. Samples were imaged on a confocal system and analyzed with an automated foci detection algorithm. Scale bar: 10 µm. (B) 53BP1–mEGFP distribution between nucleoplasmic (gray) and foci (black) fraction at increasing Zeocin concentrations. Data are the mean±s.d. of $n\geq3$. (C–E) Distribution of number of foci per cell (C), molecules per focus (D) and total amount of protein per cell expressed as number of molecules (E) for 53BP1 (green) and RIF1 (magenta). (F) Number of 53BP1–mEGFP foci co-localizing (Col; green) or not (Not Col; green striped) with RIF1. In C–F, data are plotted as mean±s.d. Dots indicate the median values for each of $n\geq3$ experiments, with $n>200$ cells per condition per replicate. ns, not significant; *$P\leq0.05$; **$P\leq0.01$; ***$P\leq0.001$; ****$P\leq0.0001$ (one-way ANOVA with Tukey's post-hoc test).

We demonstrated the applicability of SpIDA using both fluorescent proteins and immunofluorescence, the latter often representing the only option to follow protein accumulations dynamics (for example, in the context of analyses of *ex vivo* tissue samples). However, although SpIDA allows data reproducibility and inter-experimental comparison, immunolabeling might underestimate the real number of

Journal of Cell Science (2025) 138, jcs263483. doi:10.1242/jcs.263483

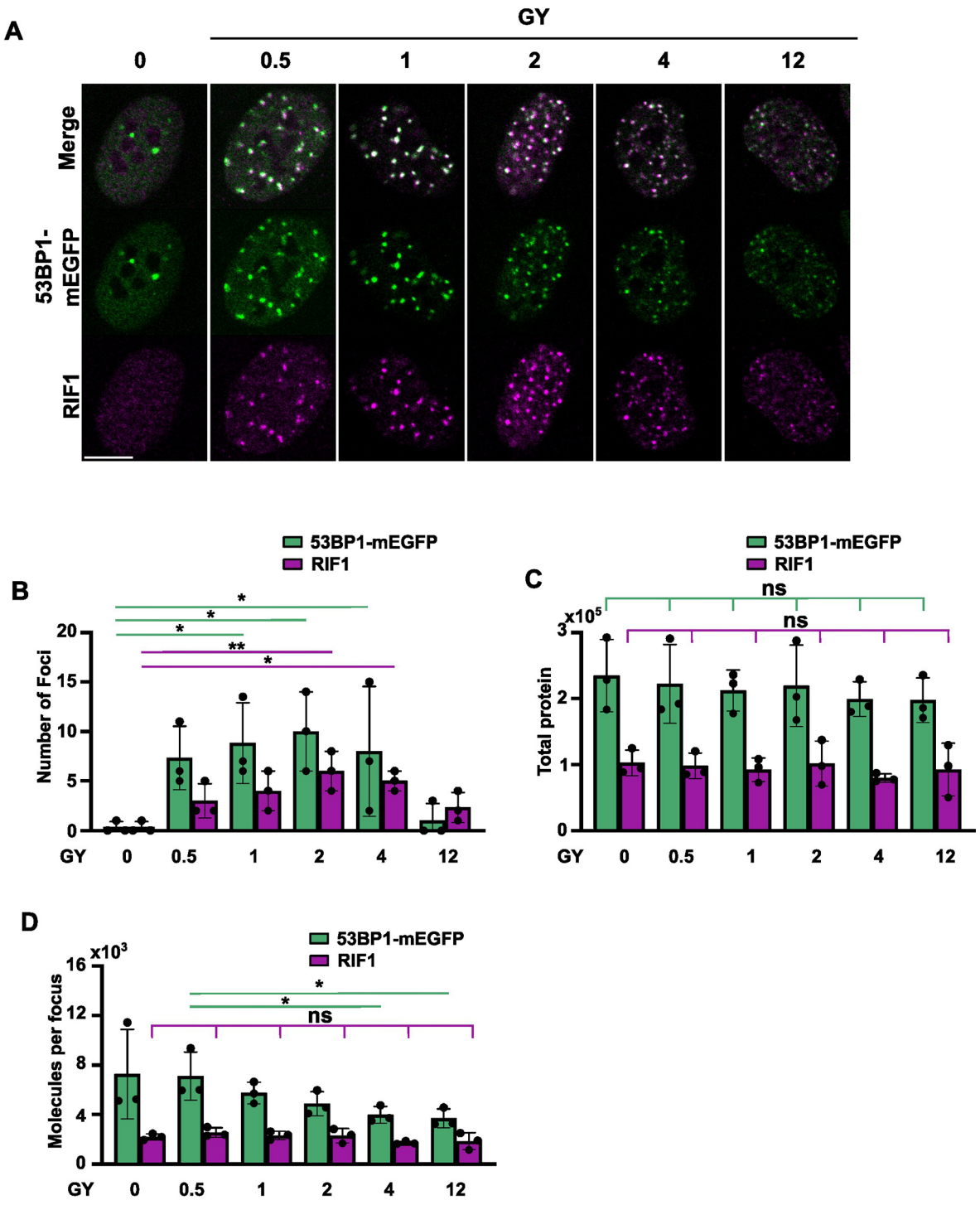

Fig. 7. 53BP1 and RIF1 show different accumulation dynamics at repair foci upon treatment with increasing IR doses. (A) 53BP1 and RIF1 focus formation in response to increasing IR-induced DNA damage load. 53BP1–mEGFP$^{+/+}$ cells were treated with the indicated IR dose, incubated for 30 min and then fixed using 4% PFA. Immunofluorescence was performed using an anti-RIF1 rabbit recombinant monoclonal antibody. Samples were imaged on a confocal system and analyzed with an automated foci detection algorithm. Scale bar: 10 µm. (B–D) Distribution of number of foci per cell (B), total amount of protein per cell expressed as number of molecules (C) and number of molecules per focus (D) for 53BP1 (green) and RIF1 (magenta). Data are plotted as mean±s.d. Dots indicate the median values for each of n=3 experiments, with n>200 cells per condition per replicate. ns, not significant; *P≤0.05; **P≤0.01 (one-way ANOVA with Tukey's post-hoc test).

molecules in the sample that we analyzed. Indeed, we observed a ∼2-fold lower calculated number of 53BP1 molecules per focus when using antibodies compared to values obtained using fluorescent proteins. This likely reflects a combination of issues affecting immunolabeling; for example, a single antibody can bind two antigens, whereas steric hindrance can reduce the accessibility of the epitope for binding to the antibody in the context of foci. Because of this, the use of monovalent, fluorescently conjugated antibodies would be expected to maximize epitope detection, thereby improving the precision of the estimation of molecule numbers.

Journal of Cell Science (2025) 138, jcs263483. doi:10.1242/jcs.263483

We showed that when the availability of 53BP1 is reduced below physiological levels, the number of 53BP1 molecules per focus decreases from ∼4200 to ∼1500. This lower threshold does not depend on the detection limit of the imaging system used, since when the analysis was performed on a heterozygous clone in which half of 53BP1 alleles were not GFP-tagged, we were still able to detect foci containing around half of this number of molecules. Finally, we showed that reducing the availability of 53BP1 by overexpressing NuMA leads to the formation of a reduced number of foci per cell, each containing around 1000 fewer molecules (from ∼4500 to ∼3500). We also observed a comparable reduction in the number of molecules per focus when cells were exposed to higher DNA damage load (∼3800 molecules at 5000 µg/ml Zeocin). Interestingly, such decrease is not due to exhaustion of nucleoplasmic pools of 53BP1, since our data reveal that the majority of 53BP1 molecules remain in the nucleoplasm at all doses tested. Future work is required to test whether reducing the interaction with NuMA or Lamin B1, for example by downregulating their expression, would maintain a stable number of molecules of 53BP1 per focus at increasing DNA damage load.

RIF1 also displayed a reduction in foci number, albeit without significant changes in the number of molecules per focus, either in conditions where the availability of 53BP1 was reduced (i.e. via siRNA) or in the presence of elevated DNA damage load (i.e. increasing Zeocin concentration or IR doses). The data suggest that, in the context of DNA repair, the number of molecules per focus of 53BP1 displays more flexibility than that of RIF1. It has been previously shown that decrease in 53BP1 availability elevates the number of replication protein A (RPA)- and Rad51-positive foci after IR exposure (Kakarougkas et al., 2013). Our data show that residual 53BP1 foci in siRNA-treated cells, despite displaying a reduced number of molecules per focus, present the same number of RIF1 molecules. However, technical limitations related to antibody combinations and compatibility with immunofluorescence prevented us from evaluating the recruitment of RPA or Rad51 at such residual 53BP1-containing foci. Thus, whether these foci retain the same anti-resection activity as the ones observed in control cells remains to be clarified.

Although our immunofluorescence data also suggest that 53BP1 and RIF1 are generally present in similar numbers of molecules in repair foci, given the limitation of the immunolabeling approach discussed above, we cannot exclude the possibility that the calculated number of RIF1 molecules present at 53BP1 foci was underestimated. Furthermore, it is unclear whether epitope accessibility is comparable for these proteins within foci. Overall, our data suggest that comparison of protein numbers in foci using immunofluorescence must be interpreted with caution. A more definitive answer with regards to the stoichiometry of these factors in DSB repair foci could be obtained by applying SpIDA on an engineered cell line where both 53BP1 and RIF1 are endogenously tagged with fluorescent protein. In this work we limited our analysis to RIF1; we also note that additional work would be necessary to evaluate whether PTIP recruitment and activity is affected by the reduced number of molecules of 53BP1 present in foci.

In addition to its role in recruiting anti-resection factors to antagonize homologous recombination, 53BP1 coordinates DSB movements by interacting with the linker of nucleoskeleton and cytoskeleton (LINC) complex, a protein that bridges chromatin and microtubules (Lottersberger et al., 2015). This interaction promotes increased mobility of dysfunctional telomeres (Dimitrova et al., 2008), and it is required for long-range variable (diversity) joining [V(D)J] recombination (Difilippantonio et al., 2008). In this context, and with proper technical adjustments to use live imaging (see below), our approach could clarify whether alteration in the number of 53BP1 molecules per focus has an impact on the mobility of DSBs.

53BP1 undergoes liquid–liquid phase separation (Kilic et al., 2019), which presumably favors the isolation of the damaged DNA from the rest of the nucleoplasm, as well as the relocalization and aggregation of repair factors around the DSB. Independently from its DNA repair activity, 53BP1 has also been shown to phase separate with HP1α (also known as CBX5), thereby contributing to heterochromatin maintenance and genome stability. Intriguingly, heterochromatin-associated 53BP1 foci have a wider area compared to DNA repair-associated ones (Zhang et al., 2022). In our experimental conditions, when no exogenous DNA damage is induced, 53BP1 foci display up to ∼2 fold higher number of molecules compared to foci formed in cells treated with 500 µg/ml of Zeocin. However, our data do not clarify whether foci present in untreated cells represent heterochromatin-associated 53BP1 (Zhang et al., 2022) or nuclear bodies (Lukas et al., 2011; Spies et al., 2019). The quantitative aspect of 53BP1 accumulation at these sites remains poorly characterized. SpIDA for 53BP1, combined with simultaneous labeling of either HP1α or TopBP1 as markers for heterochromatin and nuclear bodies (Lukas et al., 2011; Pedersen et al., 2015), respectively, could provide answers to these questions.

We have shown the applicability of SpIDA to quantitatively describe DNA repair foci based on the analysis of confocal images and the versatility of the technique to perform well with both fluorescent proteins and immunofluorescence. Importantly, the combination of fluorescent protein and antibody labeling approaches allows for multiplexing, as we show by following the recruitment of two proteins at DSBs. The experimental setup used in this work, in particular the use of fixed sample and mEGFP as fluorescent protein, does not allow the investigation of the dynamics of foci formation and resolution. Indeed, time-course analysis on fixed samples lacks the temporal resolution required to observe foci dynamics, which can be achieved with time-lapse experiments in live cells. However, the high frequency of image acquisition requires a more stable (i.e. less easily photobleachable) fluorescent reporter than mEGFP. Several options are now available to overcome this problem, including the recently engineered green-emitting fluorescent protein StayGold (Ivorra-Molla et al., 2024) and/or the Halo–HaloTag system (Los et al., 2008).

With appropriate technical adjustments and fluorescence spectrum considerations, we anticipate that SpIDA will be useful to analyze the recruitment and stoichiometries of the multitude of factors that are recruited to DDR foci. The technique is simple and free, and easy-to-use software is available. SpIDA requires widely available microscopy platforms and will be useful to facilitate the quantification and comparison of critical biological processes.

MATERIALS AND METHODS

Cell cultures

Human U2OS cells (STR analyzed; ATCC) and derived lines (mEGFP–HA, 53BP1–mEGFP) were kept in culture in DMEM (Wisent Inc., St-Jean Baptiste, QC, Canada) supplemented with 10% FBS (Wisent Inc.), Glutamax (ThermoFisher, Waltham, MA, USA), and penicillin–streptomycin–neomycin antibiotic mixture (ThermoFisher) and routinely tested for mycoplasma contamination. Transfections were performed using Lipofectamine 3000 (ThermoFisher) diluted in Optimem (ThermoFisher) according to manufacturer instructions. For the generation of stable clones, cells were selected with 800 µg/ml G418 after transfection (ThermoFisher).

DNA damage induction

For drug-induced DNA damage, cells were treated with the indicated doses of Zeocin (ThermoFisher) for 1 h, washed, and allowed to recover in fresh medium for 1 h before paraformaldehyde (PFA; Sigma-Aldrich) fixation (4% PFA in PBS pH 7.4). IR-induced damage was performed with a 137Cs source (Gamma Cell 3000 Elan; Atomic Energy Canada) at a dose rate of 4.5×10^{-2} Gy/s.

Cloning and mutagenesis

Cloning was performed using in-house generated chemically competent cells (Mix & Go! *E. Coli* transformation kit, Zymo Research) from a bacteria strain derived by XL1-Blue (Agilent). CRISPR-Cas9-mediated knock-in of the locus of 53BP1 was performed as previously described (Sharma et al., 2018). 53BP1_top and 53BP1_bottom primers (IDT) were cloned into the pLentiCRISPRv2 plasmid (Addgene plasmid #52961, http://n2t.net/addgene:52961, RRID:Addgene_52961; deposited by Feng Zhang) (Sanjana et al., 2014) using the BsmbI restriction sites. The template for the homology-directed repair (HDR) was designed in Benchling (https://benchling.com) to add the sequence of mEGFP at the C terminus of the endogenous *53BP1* locus and synthesized into a double-stranded sequence-verified genomic block by IDT (Integrated DNA Technologies, Coralville, IA, USA). Proper integration was tested via PCR using primers 53BP1gentFw and 53BP1gentRev (ThermoFisher). qPCR on genomic DNA was used to calculate the relative number of 53BP1 alleles tagged with mEGFP in wild-type, heterozygous and homozygous clones. Experiments were performed using PowerUp SYBR Green Master Mix (ThermoFisher), TBP1 (PSMC3) was used as internal calibrator for copy number, with amplification performed using primers TBP1_Fw and TBP1_Rev (Linzmeier and Ganz, 2005) (ThermoFisher).

mEGFP was generated via mutagenesis PCR using Phusion Hot Start polymerase (ThermoFisher) and the primers EGFP_A206K_Fw and EGFP_A206K_Rev. mEGFP–HA was then obtained via PCR using Phusion Hot Start polymerase and the primers EGFPHA_Fw and EGFPHA_Rev (ThermoFisher). The mEGFP–HA reporter cell line was obtained by transfecting mEGFP–HA, followed by antibiotic selection using G418 (Thermo Fisher Scientific).

Immunofluorescence

Cells were seeded on glass coverslips (Fisher Scientific) and treated as indicated before being fixed with 4% PFA in PBS. After fixation, samples were stained with DAPI (ThermoFisher; 2.5 µg/ml in PBS) or RedDot2 (Biotium, 1:200) and mounted on microscopy slides with antifade mounting medium (Vectashield, Vectorlabs, Newark, CA, USA), or subjected to immunofluorescence. In this case, samples were permeabilized in PBS containing 0.5% Triton X-100 and blocked with 3% BSA in PBS-T (PBS, 0.05% Tween-20) for 1 h at room temperature and incubated with the indicated primary antibody diluted in PBS-T containing 0.5% BSA overnight at 4°C. Antibodies used for immunofluorescence were rabbit monoclonal anti-HA tag (1:500; #3724, Cell Signaling Technology), rabbit monoclonal anti-53BP1 (1:800; #88439, Cell Signaling Technology) and rabbit monoclonal anti-RIF1 (1:250; #95558, Cell Signaling Technology). Titration experiments were performed with anti-53BP1 and anti-RIF1 antibodies to minimize partial epitope labeling due to antibody availability (Fig. S2J, Fig. S4F).

After incubation, samples were washed three times with PBS-T and incubated for 1 h at room temperature with the matching secondary antibody diluted in PBS-T containing 0.05% BSA. Secondary antibodies were goat anti-rabbit IgG Alexa-Fluor 647 (1:1000; #A-21245, ThermoFisher) and goat anti-rabbit IgG Alexa-Fluor 546 (1:1000; #A-11035, ThermoFisher). After washing with PBS-T, samples were incubated with DAPI (2.5 µg/ml in PBS; ThermoFisher) and mounted on microscopy slides with antifade mounting medium (Vectashield, Vectorlabs).

siRNA and inhibitor treatments

Cells were seeded in a 6 cm plate, and siRNA transfection was performed 24 h after using RNAiMAx (ThermoFisher) according to manufacturer instructions. Cells were used for downstream experiments 48 h after transfection. siRNA used in this work were Mission siRNA Universal Negative Control SIC001, and SASI_Hs01_00024577 and SASI_Hs01_00024578 against 53BP1 used in a 1:1 ratio (Sigma-Aldrich, Darmstadt, Germany). For ATM inhibition, cells were treated for 30 min with the indicated concentration of KU55933 (Sigma-Aldrich), followed by Zeocin treatment in the presence of KU55933.

Immunoblotting

Cells were lysed in TNE [150 mM NaCl, 50 mM Tris-HCl, pH 7.5, 2 mM EDTA, 0.5% Triton X-100 and protease inhibitor cocktail (Thermo Fisher Scientific)]. Samples were boiled in Laemmli buffer, followed by SDS-PAGE and protein transfer using standard molecular biology protocols (reagents and equipment from Bio-Rad, Hercules, CA, USA). Immunodetection was performed using the indicated primary antibody followed by the matching horseradish peroxidase (HRP)-conjugated secondary antibody (Bio-Rad, Hercules, CA, USA). Antibodies used in this work were mouse monoclonal anti-GFP (1:1000; #66002-1, Proteintech), rabbit monoclonal anti-HA tag (1:1000; #3724, Cell Signaling Technology), rabbit monoclonal anti-RIF1 (1:1000; #95558, Cell Signaling Technology), rabbit monoclonal anti-γH2AX (1:1000; #9718, Cell Signaling Technology), rabbit monoclonal anti-53BP1 (1:1000; #88439, Cell Signaling Technology), mouse monoclonal anti-β-actin (1:1000; #66009-1, Proteintech), rabbit monoclonal anti-NuMA1 (1:1000; #A4416, ABclonal), HRP-conjugated goat anti-mouse IgG (#1706516, Bio-Rad) and HRP-conjugated goat anti-rabbit IgG (#1706515, Bio-Rad). Original blot data are shown in Fig. S8.

Automated detection of nuclear DNA repair foci

A previously developed imaging processing pipeline (Binan et al., 2019; Otsu, 1979) was adapted for automated foci detection. Cell nuclei were detected using DAPI signal by Otsu thresholding to create a mask where objects were filtered according to their size, signal and shape. Foci detection was performed by first enhancing the signal of objects the size of a focus using a band-pass filter, then local maxima were detected using a threshold calculated for each nucleus to generate an initial foci mask. In order to filter for sub-diffraction limit foci, only those of an intensity profile that fitted a Gaussian curve of a width compatible with the point spread function of the imaging system were retained for analysis. Such a quality control step was performed for each focus; poorly fitted foci, according to a predefined threshold, were not considered for further analysis. Code is available upon request.

Imaging

Samples were imaged on an inverted Olympus IX71 microscope (Olympus Corporations of the Americas, Center Valley, PA, USA) equipped with a confocal module and PMT detectors (Thorlabs Inc., Newton, NJ, USA), using a 60× objective with a 1.25 NA, or on a FV1000 LSM Olympus IX81 confocal microscope equipped with multialkali PMT detectors, using a 60× objective with a 1.4 NA.

Software

Immunofluorescence panels were created using Fiji (Schindelin et al., 2012). SpIDA and the associated software pipeline was coded using MATLAB version R2022b (The MathWorks Inc., Natick, MA, USA; www.mathworks.com). Statistical analysis was performed using GraphPad Prism version 10.2.2 for Mac (GraphPad Software, Boston, MA, USA; www.graphpad.com).

Primers

The following oligonucleotide primers were used: 53BP1 top, 5′-CACCGTGTTTCTCACTAAAGATACT-3′ (Kilic et al., 2019); 53BP1 bottom, 5′-AAACAGTATCTTTAGTGAGAAACAC-3′ (Kilic et al., 2019); 53BP1_genFw, 5′-TGCTTTAGGGGTATTTGATGTGG-3′ (Kilic et al., 2019); 53BP1_genRev, 5′-ATTCTCTGCTCCCCACCTCT-3′ (Kilic et al., 2019); EGFP_A206K_Fw, 5′-GCACCCAGTCCAAACTGAG-CAAAGA-3′; EGFP_A206K_Rev, 5′-TCAGGTAGTGGTTGTCGGG-CA-3′; EGFPHA_Fw, 5′-GGCCCGGGATCCACCGGTCGCCACCA-TGG-3′; EGFPHA_Rev, 5′-GGACGAGCTGTACAAGTACCCATACGA-TGTTCCAGATTACGTTAAGCGGCCGCTCAG-3′; TBP1_Fw, 5′-TGA-GAAGATGGATGTTGAGTTG-3′ (Linzmeier and Ganz, 2005);

TBP1_Rev, 5′-AGATAGCAGCACGGTATGAG-3′ (Linzmeier and Ganz, 2005).

Acknowledgements
We would like to thank Pierre-Alexandre Vidi (InGenO Laboratory, Institut de Cancérologie de l'Ouest, France) for kindly sharing the mCherry-NuMA plasmid, as well as the microscopy facility at the Maisonneuve-Rosemont Hospital Research Center.

Competing interests
The authors declare no competing or financial interests.

Author contributions
Conceptualization: G.M., H.W., S.C.; Formal analysis: G.M., S.C.; Funding acquisition: S.C.; Investigation: G.M., J.R.; Methodology: G.M., H.W., S.C.; Resources: S.C.; Software: G.M., J.R., A.G.G., S.C.; Supervision: S.C.; Writing – original draft: G.M.; Writing – review & editing: G.M., J.R., A.G.G., H.W., S.C.

Funding
This work was supported by grants from the Cancer Research Society of Canada (to S.C. and H.W.) and the Natural Sciences and Engineering Research Council of Canada (to S.C., H.W. and A.G.G.). A.G.G. is a scholar of the Fonds de recherche du Québec - Santé (FRQS). A.G.G. is supported by a Sentinel North Partnership Research Chair. G.M. holds a postdoctoral fellowship from FRQS.

Data and resource availability
All relevant data and details of resources can be found within the article and its supplementary information.

Peer review history
The peer review history is available online at https://journals.biologists.com/jcs/lookup/doi/10.1242/jcs.263483.reviewer-comments.pdf

References

Bakr, A., Köcher, S., Volquardsen, J., Petersen, C., Borgmann, K., Dikomey, E., Rothkamm, K. and Mansour, W. Y. (2016). Impaired 53BP1/RIF1 DSB mediated end-protection stimulates CtIP-dependent end resection and switches the repair to PARP1-dependent end joining in G1. *Oncotarget* **7**, 57679-57693. doi:10.18632/oncotarget.11023

Barbeau, A., Godin, A. G., Swift, J. L., De Koninck, Y., Wiseman, P. W. and Beaulieu, J.-M. (2013a). Quantification of receptor tyrosine kinase activation and transactivation by G-protein-coupled receptors using spatial intensity distribution analysis (SpIDA). *Methods Enzymol.* **522**, 109-131. doi:10.1016/B978-0-12-407865-9.00007-8

Barbeau, A., Swift, J. L., Godin, A. G., De Koninck, Y., Wiseman, P. W. and Beaulieu, J.-M. (2013b). Spatial intensity distribution analysis (SpIDA): a new tool for receptor tyrosine kinase activation and transactivation quantification. *Methods Cell Biol.* **117**, 1-19. doi:10.1016/B978-0-12-408143-7.00001-3

Becker, A., Durante, M., Taucher-Scholz, G. and Jakob, B. (2014). ATM alters the otherwise robust chromatin mobility at sites of DNA double-strand breaks (DSBs) in human cells. *PLoS ONE* **9**, e92640. doi:10.1371/journal.pone.0092640

Bekker-Jensen, S. and Mailand, N. (2010). Assembly and function of DNA double-strand break repair foci in mammalian cells. *DNA Repair* **9**, 1219-1228. doi:10.1016/j.dnarep.2010.09.010

Bekker-Jensen, S., Lukas, C., Melander, F., Bartek, J. and Lukas, J. (2005). Dynamic assembly and sustained retention of 53BP1 at the sites of DNA damage are controlled by Mdc1/NFBD1. *J. Cell Biol.* **170**, 201-211. doi:10.1083/jcb.200503043

Bélanger, F., Angers, J.-P., Fortier, É., Hammond-Martel, I., Costantino, S., Drobetsky, E. and Wurtele, H. (2016). Mutations in replicative stress response pathways are associated with S phase-specific defects in nucleotide excision repair. *J. Biol. Chem.* **291**, 522-537. doi:10.1074/jbc.M115.685883

Binan, L., Bélanger, F., Uriarte, M., Lemay, J. F., Pelletier De Koninck, J. C., Roy, J., Affar, E. B., Drobetsky, E., Wurtele, H. and Costantino, S. (2019). Opto-magnetic capture of individual cells based on visual phenotypes. *eLife* **8**, e45239. doi:10.7554/eLife.45239

Boersma, V., Moatti, N., Segura-Bayona, S., Peuscher, M. H., Van Der Torre, J., Wevers, B. A., Orthwein, A., Durocher, D. and Jacobs, J. J. L. (2015). MAD2L2 controls DNA repair at telomeres and DNA breaks by inhibiting 5′ end resection. *Nature* **521**, 537-540. doi:10.1038/nature14216

Bothmer, A., Robbiani, D. F., Feldhahn, N., Gazumyan, A., Nussenzweig, A. and Nussenzweig, M. C. (2010). 53BP1 regulates DNA resection and the choice between classical and alternative end joining during class switch recombination. *J. Cell Biol.* **189**, i3. doi:10.1083/JCB1892OIA3

Botuyan, M. V., Lee, J., Ward, I. M., Kim, J.-E., Thompson, J. R., Chen, J. and Mer, G. (2006). Structural basis for the methylation state-specific recognition of histone H4-K20 by 53BP1 and Crb2 in DNA repair. *Cell* **127**, 1361-1373. doi:10.1016/j.cell.2006.10.043

Bouwman, P., Aly, A., Escandell, J. M., Pieterse, M., Bartkova, J., Van Der Gulden, H., Hiddingh, S., Thanasoula, M., Kulkarni, A., Yang, Q. et al. (2010). 53BP1 loss rescues BRCA1 deficiency and is associated with triple-negative and BRCA-mutated breast cancers. *Nat. Struct. Mol. Biol.* **17**, 688-695. doi:10.1038/nsmb.1831

Bunting, S. F., Callén, E., Wong, N., Chen, H.-T., Polato, F., Gunn, A., Bothmer, A., Feldhahn, N., Fernandez-Capetillo, O., Cao, L. et al. (2010). 53BP1 inhibits homologous recombination in Brca1-deficient cells by blocking resection of DNA breaks. *Cell* **141**, 243-254. doi:10.1016/j.cell.2010.03.012

Buzza, K. M., Pluen, A., Doherty, C., Cheesapcharoen, T., Singh, G., Ledder, R. G., Sreenivasan, P. K. and McBain, A. J. (2023). Modulation of biofilm formation and permeability in Streptococcus mutans during exposure to zinc acetate. *Microbiol. Spectrum* **11**, e0252722. doi:10.1128/spectrum.02527-22

Callen, E., Di Virgilio, M., Kruhlak, M. J., Nieto-Soler, M., Wong, N., Chen, H.-T., Faryabi, R. B., Polato, F., Santos, M., Starnes, L. M. et al. (2013). 53BP1 mediates productive and mutagenic DNA repair through distinct phosphoprotein interactions. *Cell* **153**, 1266-1280. doi:10.1016/j.cell.2013.05.023

Callen, E., Zong, D., Wu, W., Wong, N., Stanlie, A., Ishikawa, M., Pavani, R., Dumitrache, L. C., Byrum, A. K., Mendez-Dorantes, C. et al. (2020). 53BP1 enforces distinct pre- and post-resection blocks on homologous recombination. *Mol. Cell* **77**, 26-38.e7. doi:10.1016/j.molcel.2019.09.024

Chapman, J. R., Barral, P., Vannier, J.-B., Borel, V., Steger, M., Tomas-Loba, A., Sartori, A. A., Adams, I. R., Batista, F. D. and Boulton, S. J. (2013). RIF1 is essential for 53BP1-dependent nonhomologous end joining and suppression of DNA double-strand break resection. *Mol. Cell* **49**, 858-871. doi:10.1016/j.molcel.2013.01.002

Ciccia, A. and Elledge, S. J. (2010). The DNA damage response: making it safe to play with knives. *Mol. Cell* **40**, 179-204. doi:10.1016/j.molcel.2010.09.019

Cranfill, P. J., Sell, B. R., Baird, M. A., Allen, J. R., Lavagnino, Z., De Gruiter, H. M., Kremers, G.-J., Davidson, M. W., Ustione, A. and Piston, D. W. (2016). Quantitative assessment of fluorescent proteins. *Nat. Methods* **13**, 557-562. doi:10.1038/nmeth.3891

Dev, H., Chiang, T.-W. W., Lescale, C., de Krijger, I., Martin, A. G., Pilger, D., Coates, J., Sczaniecka-Clift, M., Wei, W., Ostermaier, M. et al. (2018). Shieldin complex promotes DNA end-joining and counters homologous recombination in BRCA1-null cells. *Nat. Cell Biol.* **20**, 954-965. doi:10.1038/s41556-018-0140-1

Di Virgilio, M., Callen, E., Yamane, A., Zhang, W., Jankovic, M., Gitlin, A. D., Feldhahn, N., Resch, W., Oliveira, T. Y., Chait, B. T. et al. (2013). Rif1 prevents resection of DNA breaks and promotes immunoglobulin class switching. *Science* **339**, 711-715. doi:10.1126/science.1230624

Difilippantonio, S., Gapud, E., Wong, N., Huang, C.-Y., Mahowald, G., Chen, H. T., Kruhlak, M. J., Callen, E., Livak, F., Nussenzweig, M. C. et al. (2008). 53BP1 facilitates long-range DNA end-joining during V(D)J recombination. *Nature* **456**, 529-533. doi:10.1038/nature07476

Dimitrova, N., Chen, Y.-C. M., Spector, D. L. and de Lange, T. (2008). 53BP1 promotes non-homologous end joining of telomeres by increasing chromatin mobility. *Nature* **456**, 524-528. doi:10.1038/nature07433

Escribano-Díaz, C., Orthwein, A., Fradet-Turcotte, A., Xing, M., Young, J. T. F., Tkáč, J., Cook, M. A., Rosebrock, A. P., Munro, M., Canny, M. D. et al. (2013). A cell cycle-dependent regulatory circuit composed of 53BP1-RIF1 and BRCA1-CtIP controls DNA repair pathway choice. *Mol. Cell* **49**, 872-883. doi:10.1016/j.molcel.2013.01.001

Etourneaud, L., Moussa, A., Rass, E., Genet, D., Willaume, S., Chabance-Okumura, C., Wanschoor, P., Picotto, J., Thézé, B., Dépagne, J. et al. (2021). Lamin B1 sequesters 53BP1 to control its recruitment to DNA damage. *Sci. Adv.* **7**, eabb3799. doi:10.1126/sciadv.abb3799

Findlay, S., Heath, J., Luo, V. M., Malina, A., Morin, T., Coulombe, Y., Djerir, B., Li, Z., Samiei, A., Simo-Cheyou, E. et al. (2018). SHLD2/FAM35A co-operates with REV7 to coordinate DNA double-strand break repair pathway choice. *EMBO J.* **37**, e100158. doi:10.15252/embj.2018100158

Fradet-Turcotte, A., Canny, M. D., Escribano-Díaz, C., Orthwein, A., Leung, C. C. Y., Huang, H., Landry, M.-C., Kitevski-Leblanc, J., Noordermeer, S. M., Sicheri, F. et al. (2013). 53BP1 is a reader of the DNA-damage-induced H2A Lys 15 ubiquitin mark. *Nature* **499**, 50-54. doi:10.1038/nature12318

Gatti, M., Pinato, S., Maspero, E., Soffientini, P., Polo, S. and Penengo, L. (2012). A novel ubiquitin mark at the N-terminal tail of histone H2As targeted by RNF168 ubiquitin ligase. *Cell Cycle* **11**, 2538-2544. doi:10.4161/cc.20919

Ghezraoui, H., Oliveira, C., Becker, J. R., Bilham, K., Moralli, D., Anzilotti, C., Fischer, R., Deobagkar-Lele, M., Sanchiz-Calvo, M., Fueyo-Marcos, E. et al. (2018). 53BP1 cooperation with the REV7–shieldin complex underpins DNA structure-specific NHEJ. *Nature* **560**, 122-127. doi:10.1038/s41586-018-0362-1

Godin, A. G., Costantino, S., Lorenzo, L.-E., Swift, J. L., Sergeev, M., Ribeiro-Da-Silva, A., De Koninck, Y. and Wiseman, P. W. (2011). Revealing protein oligomerization and densities in situ using spatial intensity distribution analysis. *Proc. Natl. Acad. Sci. USA* **108**, 7010-7015. doi:10.1073/pnas.1018658108

Gudjonsson, T., Altmeyer, M., Savic, V., Toledo, L., Dinant, C., Grøfte, M., Bartkova, J., Poulsen, M., Oka, Y., Bekker-Jensen, S. et al. (2012). TRIP12 and

UBR5 suppress spreading of chromatin ubiquitylation at damaged chromosomes. *Cell* **150**, 697-709. doi:10.1016/j.cell.2012.06.039

Gupta, R., Somyajit, K., Narita, T., Maskey, E., Stanlie, A., Kremer, M., Typas, D., Lammers, M., Mailand, N., Nussenzweig, A. et al. (2018). DNA repair network analysis reveals shieldin as a key regulator of NHEJ and PARP inhibitor sensitivity. *Cell* **173**, 972-988.e23. doi:10.1016/j.cell.2018.03.050

Haaf, T., Golub, E. I., Reddy, G., Radding, C. M. and Ward, D. C. (1995). Nuclear foci of mammalian Rad51 recombination protein in somatic cells after DNA damage and its localization in synaptonemal complexes. *Proc. Natl. Acad. Sci. U.S.A.* **92**, 2298-2302. doi:10.1073/pnas.92.6.2298

Hamrang, Z., McGlynn, H. J., Clarke, D., Penny, J. and Pluen, A. (2014). Monitoring the kinetics of CellTrace™ calcein red-orange AM intracellular accumulation with spatial intensity distribution analysis. *Biochim. Biophys. Acta* **1840**, 2914-2923. doi:10.1016/j.bbagen.2014.05.014

Harding, S. M., Coackley, C. and Bristow, R. G. (2011). ATM-dependent phosphorylation of 53BP1 in response to genomic stress in oxic and hypoxic cells. *Radiother. Oncol.* **99**, 307-312. doi:10.1016/j.radonc.2011.05.039

Harrigan, J. A., Belotserkovskaya, R., Coates, J., Dimitrova, D. S., Polo, S. E., Bradshaw, C. R., Fraser, P. and Jackson, S. P. (2011). Replication stress induces 53BP1-containing OPT domains in G1 cells. *J. Cell Biol.* **193**, 97-108. doi:10.1083/jcb.201011083

Isbilir, A., Moller, J., Arimont, M., Bobkov, V., Perpina-Viciano, C., Hoffmann, C., Inoue, A., Heukers, R., De Graaf, C., Smit, M. J. et al. (2020). Advanced fluorescence microscopy reveals disruption of dynamic CXCR4 dimerization by subpocket-specific inverse agonists. *Proc. Natl. Acad. Sci. USA* **117**, 29144-29154. doi:10.1073/pnas.2013319117

Ivorra-Molla, E., Akhuli, D., McAndrew, M. B. L., Scott, W., Kumar, L., Palani, S., Mishima, M., Crow, A. and Balasubramanian, M. K. (2024). A monomeric StayGold fluorescent protein. *Nat. Biotechnol.* **42**, 1368-1371. doi:10.1038/s41587-023-02018-w

Jackson, S. P. and Bartek, J. (2009). The DNA-damage response in human biology and disease. *Nature* **461**, 1071-1078. doi:10.1038/nature08467

Kakarougkas, A., Ismail, A., Klement, K., Goodarzi, A. A., Conrad, S., Freire, R., Shibata, A., Lobrich, M. and Jeggo, P. A. (2013). Opposing roles for 53BP1 during homologous recombination. *Nucleic Acids Res.* **41**, 9719-9731. doi:10.1093/nar/gkt729

Kilic, S., Lezaja, A., Gatti, M., Bianco, E., Michelena, J., Imhof, R. and Altmeyer, M. (2019). Phase separation of 53BP1 determines liquid-like behavior of DNA repair compartments. *EMBO J.* **38**, e101379. doi:10.15252/embj.2018101379

Kleiner, R. E., Verma, P., Molloy, K. R., Chait, B. T. and Kapoor, T. M. (2015). Chemical proteomics reveals a γH2AX-53BP1 interaction in the DNA damage response. *Nat. Chem. Biol.* **11**, 807-814. doi:10.1038/nchembio.1908

Lambert, T. J. and Waters, J. C. (2017). Navigating challenges in the application of superresolution microscopy. *J. Cell Biol.* **216**, 53-63. doi:10.1083/jcb.201610011

Linzmeier, R. M. and Ganz, T. (2005). Human defensin gene copy number polymorphisms: comprehensive analysis of independent variation in alpha- and beta-defensin regions at 8p22-p23. *Genomics* **86**, 423-430. doi:10.1016/j.ygeno.2005.06.003

Los, G. V., Encell, L. P., McDougall, M. G., Hartzell, D. D., Karassina, N., Zimprich, C., Wood, M. G., Learish, R., Ohana, R. F., Urh, M. et al. (2008). HaloTag: a novel protein labeling technology for cell imaging and protein analysis. *ACS Chem. Biol.* **3**, 373-382. doi:10.1021/cb800025k

Lottersberger, F., Karssemeijer, R. A., Dimitrova, N. and de Lange, T. (2015). 53BP1 and the LINC complex promote microtubule-dependent DSB mobility and DNA repair. *Cell* **163**, 880-893. doi:10.1016/j.cell.2015.09.057

Lukas, C., Savic, V., Bekker-Jensen, S., Doil, C., Neumann, B., Pedersen, R. S., Grøfte, M., Chan, K. L., Hickson, I. D., Bartek, J. et al. (2011). 53BP1 nuclear bodies form around DNA lesions generated by mitotic transmission of chromosomes under replication stress. *Nat. Cell Biol.* **13**, 243-253. doi:10.1038/ncb2201

Maser, R. S., Monsen, K. J., Nelms, B. E. and Petrini, J. H. J. (1997). hMre11 and hRad50 nuclear foci are induced during the normal cellular response to DNA double-strand breaks. *Mol. Cell. Biol.* **17**, 6087-6096. doi:10.1128/MCB.17.10.6087

Meador, J. A., Morris, R. J. and Balajee, A. S. (2022). Ionizing radiation-induced DNA damage response in primary melanocytes and keratinocytes of human skin. *Cytogenet Genome Res.* **162**, 188-200. doi:10.1159/000527037

Mirman, Z., Lottersberger, F., Takai, H., Kibe, T., Gong, Y., Takai, K., Bianchi, A., Zimmermann, M., Durocher, D. and De Lange, T. (2018). 53BP1–RIF1–shieldin counteracts DSB resection through CST- and Polα-dependent fill-in. *Nature* **560**, 112-116. doi:10.1038/s41586-018-0324-7

Mok, M. T. S. and Henderson, B. R. (2012a). The in vivo dynamic interplay of MDC1 and 53BP1 at DNA damage-induced nuclear foci. *Int. J. Biochem. Cell Biol.* **44**, 1398-1409. doi:10.1016/j.biocel.2012.05.025

Mok, M. T. S. and Henderson, B. R. (2012b). The in vivo dynamic organization of BRCA1-A complex proteins at DNA damage-induced nuclear foci. *Traffic* **13**, 800-814. doi:10.1111/j.1600-0854.2012.01355.x

Munoz, I. M., Jowsey, P. A., Toth, R. and Rouse, J. (2007). Phospho-epitope binding by the BRCT domains of hPTIP controls multiple aspects of the cellular response to DNA damage. *Nucleic Acids Res.* **35**, 5312-5322. doi:10.1093/nar/gkm493

Noordermeer, S. M., Adam, S., Setiaputra, D., Barazas, M., Pettitt, S. J., Ling, A. K., Olivieri, M., Álvarez-Quilón, A., Moatti, N., Zimmermann, M. et al. (2018). The shieldin complex mediates 53BP1-dependent DNA repair. *Nature* **560**, 117-121. doi:10.1038/s41586-018-0340-7

Ochs, F., Somyajit, K., Altmeyer, M., Rask, M.-B., Lukas, J. and Lukas, C. (2016). 53BP1 fosters fidelity of homology-directed DNA repair. *Nat. Struct. Mol. Biol.* **23**, 714-721. doi:10.1038/nsmb.3251

Ochs, F., Karemore, G., Miron, E., Brown, J., Sedlackova, H., Rask, M.-B., Lampe, M., Buckle, V., Schermelleh, L., Lukas, J. et al. (2019). Stabilization of chromatin topology safeguards genome integrity. *Nature* **574**, 571-574. doi:10.1038/s41586-019-1659-4

Otsu, N. (1979). A threshold selection method from gray-level histograms. *IEEE Trans. Syst. Man Cybernet.* **9**, 62-66. doi:10.1109/TSMC.1979.4310076

Pedersen, R. T., Kruse, T., Nilsson, J., Oestergaard, V. H. and Lisby, M. (2015). TopBP1 is required at mitosis to reduce transmission of DNA damage to G1 daughter cells. *J. Cell Biol.* **210**, 565-582. doi:10.1083/jcb.201502107

Salvador Moreno, N., Liu, J., Haas, K. M., Parker, L. L., Chakraborty, C., Kron, S. J., Hodges, K., Miller, L. D., Langefeld, C., Robinson, P. J. et al. (2019). The nuclear structural protein NuMA is a negative regulator of 53BP1 in DNA double-strand break repair. *Nucleic Acids Res.* **47**, 2703-2715. doi:10.1093/nar/gkz138

Sanjana, N. E., Shalem, O. and Zhang, F. (2014). Improved vectors and genome-wide libraries for CRISPR screening. *Nat. Methods* **11**, 783-784. doi:10.1038/nmeth.3047

Schindelin, J., Arganda-Carreras, I., Frise, E., Kaynig, V., Longair, M., Pietzsch, T., Preibisch, S., Rueden, C., Saalfeld, S., Schmid, B. et al. (2012). Fiji: an open-source platform for biological-image analysis. *Nat. Methods* **9**, 676-682. doi:10.1038/nmeth.2019

Scully, R., Panday, A., Elango, R. and Willis, N. A. (2019). DNA double-strand break repair-pathway choice in somatic mammalian cells. *Nat. Rev. Mol. Cell Biol.* **20**, 698-714. doi:10.1038/s41580-019-0152-0

Sergeev, M., Godin, A. G., Kao, L., Abuladze, N., Wiseman, P. W. and Kurtz, I. (2012a). Determination of membrane protein transporter oligomerization in native tissue using spatial fluorescence intensity fluctuation analysis. *PLoS ONE* **7**, e36215. doi:10.1371/journal.pone.0036215

Sergeev, M., Swift, J. L., Godin, A. G. and Wiseman, P. W. (2012b). Ligand-induced clustering of EGF receptors: a quantitative study by fluorescence image moment analysis. *Biophys. Chem.* **161**, 50-53. doi:10.1016/j.bpc.2011.11.003

Setiaputra, D. and Durocher, D. (2019). Shieldin - the protector of DNA ends. *EMBO Rep.* **20**, e47560. doi:10.15252/embr.201847560

Setiaputra, D., Escribano-Díaz, C., Reinert, J. K., Sadana, P., Zong, D., Callen, E., Sifri, C., Seebacher, J., Nussenzweig, A., Thomä, N. H. et al. (2022). RIF1 acts in DNA repair through phosphopeptide recognition of 53BP1. *Mol. Cell* **82**, 1359-1371.e9. doi:10.1016/j.molcel.2022.01.025

Sharma, A., Toepfer, C. N., Ward, T., Wasson, L., Agarwal, R., Conner, D. A., Hu, J. H. and Seidman, C. E. (2018). CRISPR/Cas9-mediated fluorescent tagging of endogenous proteins in human pluripotent stem cells. *Curr. Protoc. Hum. Genet.* **96**, 21.11.1-21.11.20. doi:10.1002/cphg.52

Spegg, V. and Altmeyer, M. (2021). Biomolecular condensates at sites of DNA damage: more than just a phase. *DNA Repair* **106**, 103179. doi:10.1016/j.dnarep.2021.103179

Spies, J., Lukas, C., Somyajit, K., Rask, M.-B., Lukas, J. and Neelsen, K. J. (2019). 53BP1 nuclear bodies enforce replication timing at under-replicated DNA to limit heritable DNA damage. *Nat. Cell Biol.* **21**, 487-497. doi:10.1038/s41556-019-0293-6

Swift, J. L., Godin, A. G., Doré, K., Freland, L., Bouchard, N., Nimmo, C., Sergeev, M., De Koninck, Y., Wiseman, P. W. and Beaulieu, J.-M. (2011). Quantification of receptor tyrosine kinase transactivation through direct dimerization and surface density measurements in single cells. *Proc. Natl. Acad. Sci. USA* **108**, 7016-7021. doi:10.1073/pnas.1018280108

Varga, D., Majoros, H., Ujfaludi, Z., Erdélyi, M. and Pankotai, T. (2019). Quantification of DNA damage induced repair focus formation via super-resolution dSTORM localization microscopy. *Nanoscale* **11**, 14226-14236. doi:10.1039/C9NR03696B

Ward, R. J., Pediani, J. D., Godin, A. G. and Milligan, G. (2015). Regulation of oligomeric organization of the serotonin 5-hydroxytryptamine 2C (5-HT2C) receptor observed by spatial intensity distribution analysis. *J. Biol. Chem.* **290**, 12844-12857. doi:10.1074/jbc.M115.644724

Xu, G., Chapman, J. R., Brandsma, I., Yuan, J., Mistrik, M., Bouwman, P., Bartkova, J., Gogola, E., Warmerdam, D., Barazas, M. et al. (2015). REV7 counteracts DNA double-strand break resection and affects PARP inhibition. *Nature* **521**, 541-544. doi:10.1038/nature14328

Zhang, L., Geng, X., Wang, F., Tang, J., Ichida, Y., Sharma, A., Jin, S., Chen, M., Tang, M., Pozo, F. M. et al. (2022). 53BP1 regulates heterochromatin through liquid phase separation. *Nat. Commun.* **13**, 360. doi:10.1038/s41467-022-28019-y

Zimmermann, M., Lottersberger, F., Buonomo, S. B., Sfeir, A. and De Lange, T. (2013). 53BP1 regulates DSB repair using Rif1 to control 5′ end resection. *Science* **339**, 700-704. doi:10.1126/science.1231573

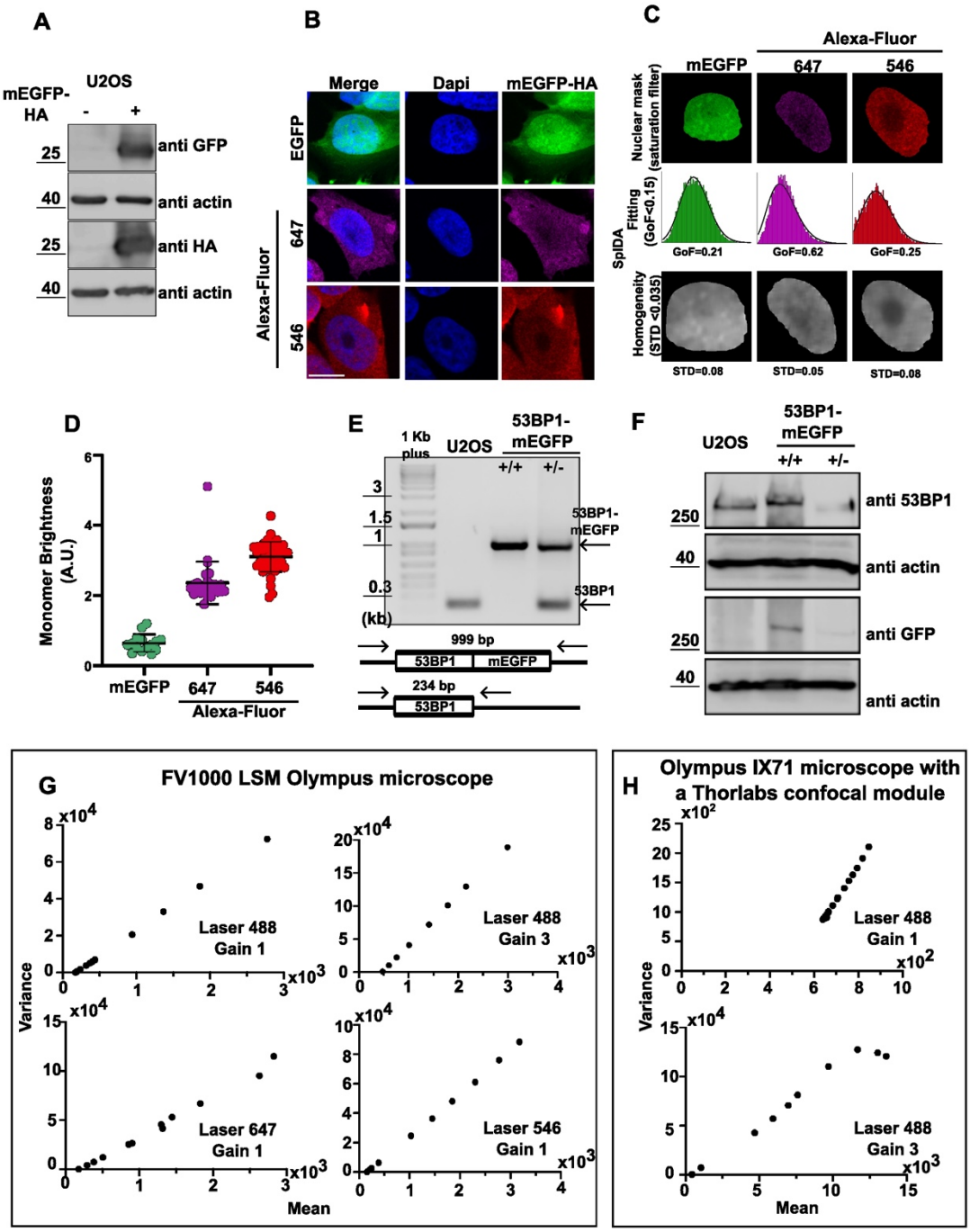

Fig. S1. (A) Immunoblot validation of mEGFP-HA reporter cell line. Cell lysates were loaded on a 12% SDS-PAGE and blotted with anti-GFP, anti-HA, or anti-actin antibodies. (B) Examples of nuclei not suitable for SpIDA. U2OS stably expressing mEGFP-HA were fixed and immunofluorescence with antibody against HA was performed, using secondary antibody conjugated with Alexa-Fluor 647 (middle) or Alexa-Fluor 546 (bottom) as indicated. DAPI is used as a nuclear marker (Blue). (C) SpIDA image processing. DAPI signal is used to segment nuclei and images are filtered to eliminate cells with saturated pixels (top row). Examples of discarded (GoF>0.15) pixel distribution histograms with the relative fitted curves (middle row) and heterogeneous nuclei (STD>0.035) (bottom row) are shown in each channel. (D) Representative distribution of SpIDA monomer brightness output in the indicated channel, with reported mean and standard deviation (E) PCR genotyping of U2OS, 53BP1-mEGFP homo (+/+) and heterozygous (+/-) clones. mEGFP was added before the stop codon on exon 28. Ladder: 1KB plus (ThermoFisher) (F) Immunoblot validation of 53BP1-mEGFP clones. Cell lysates were loaded on a 6%-12% double-gradient SDS-PAGE and blotted with anti-53BP1, anti-GFP, or anti-actin antibodies. (G-H) Noise profile of the photodetectors used for SpIDA. For each indicated CLSM set up, images of the response of the detector to reflected laser light at increasing laser power are collected. Plots show the intensity variance as function of a mean intensity collected on the detector of the indicated confocal system. A.U., arbitrary units. Scale bar 10 μm.

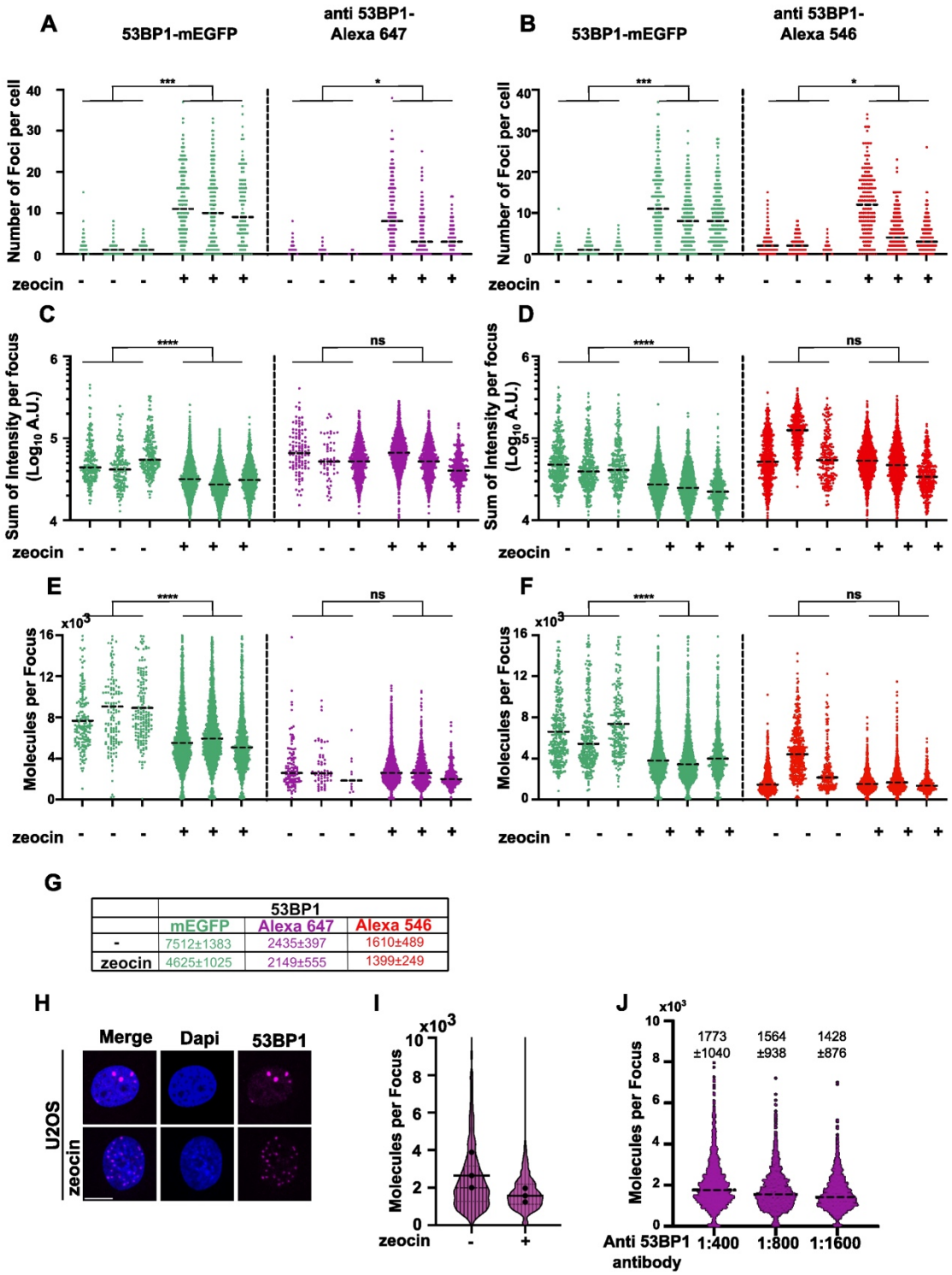

Fig. S2. Individual data point distribution of (A-B) number of foci per cell, (C-D) sum of intensity per focus, (E-F) molecules per focus of 53BP1-mEGFP calculated in GFP and Alexa-fluor 647 channel, or GFP Alexa-fluor 546 channel. Data show distribution of three replicates as a complement for bar plots shown in Figure 1. Dotted line represents the mean. (G) Average molecules per focus calculated for 53BP1 in GFP, Alexa-Fluor 647 and Alexa-Fluor 546 channels. (H) U2OS cells are treated or not with with 500 µg/mL zeocin as indicated. IF is performed using a monoclonal antibody against 53BP1 and a secondary antibody conjugated with Alexa-Fluor 647. (I) Number of molecules per focus of endogenous 53BP1 in U2OS cells. Violin plots are an illustrative example of one experiment. Black dots indicate the median values of n=3 replicates, n>200 cells per condition. (J) Number of molecules per focus of endogenous 53BP1 in U2OS calculated using the indicated antibody concentrations, dotted lines represent the mean. Calculated median number of molecules per focus is indicated for each condition.
Statistical analysis was performed on the median. A.U., arbitrary units, ns, not significant, *P≤0.05, ***P≤0.001,****P≤0.0001; unpaired, two-tailed Student t-test. Scale bar 10 µm

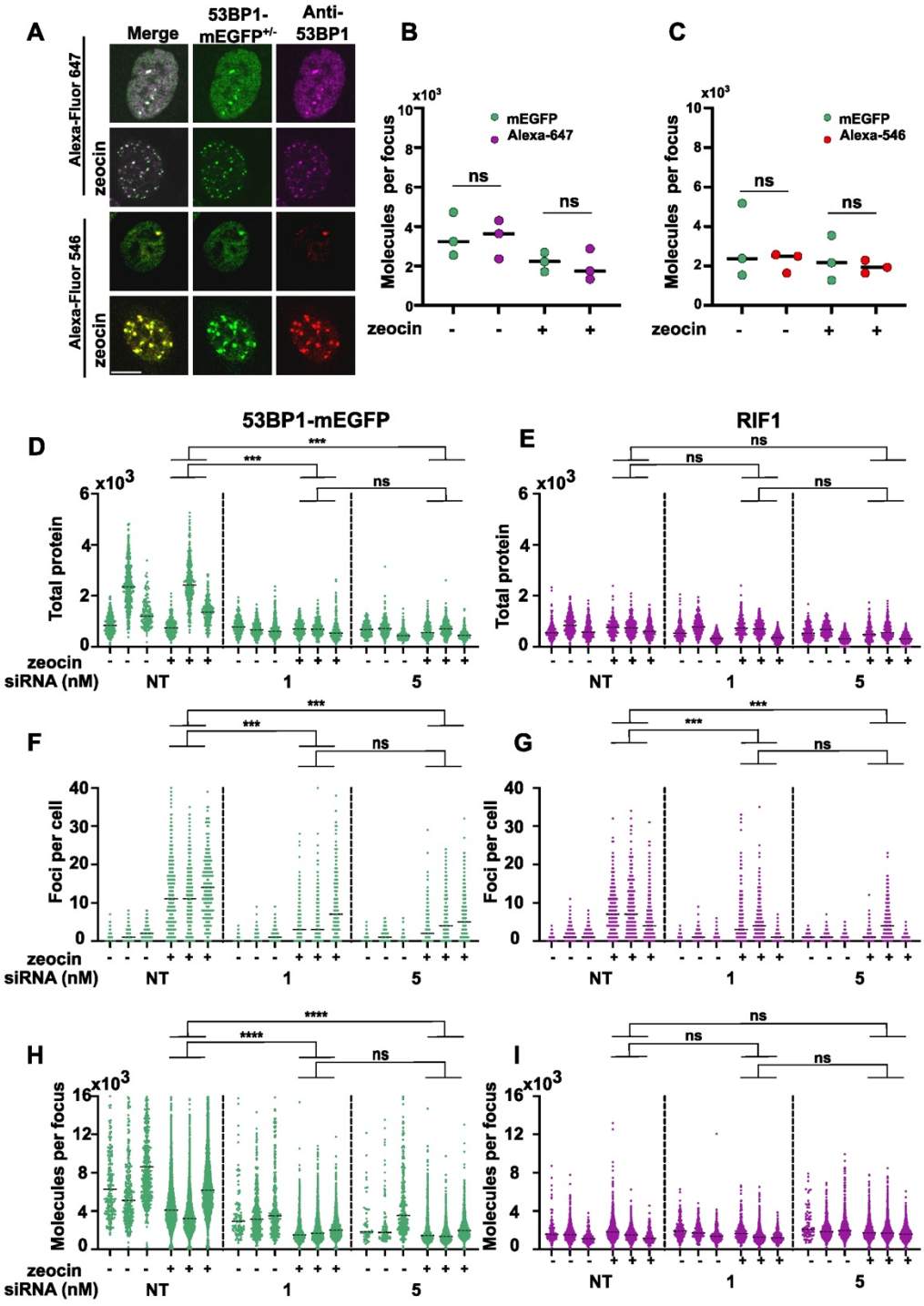

Fig. S3. (A) 53BP1-mEGFP$^{+/-}$ cells are treated or not with 500 µg/mL zeocin as indicated. IF is performed using a monoclonal antibody against 53BP1 and a secondary antibody conjugated either with Alexa-Fluor 647 or Alexa-Fluor 546 as indicated. (B-C) Comparison of median number of molecules per focus of n=3 replicates for (B) mEGFP and Alexa-Fluor 647 and (C) mEGFP and Alexa-Fluor 546. (D-I) Individual data point distribution of (D-E) total number of molecules in the focal plane, (F-G) number of foci per cell, (H-I) molecules per focus of respectively 53BP1-mEGFP and RIF1. Data set shows distribution of three replicates as a complement for the bar plots shown in figure 3. Dotted line represents the mean. Statistical analysis was performed on the median. ns, not significant, **P≤0.01, ***P≤0.001, ****P≤0.0001; (B-C) unpaired, two-tailed Student t-test, (D-I) one-way ANOVA with Tukey's post-hoc test. Scale bar 10 µm.

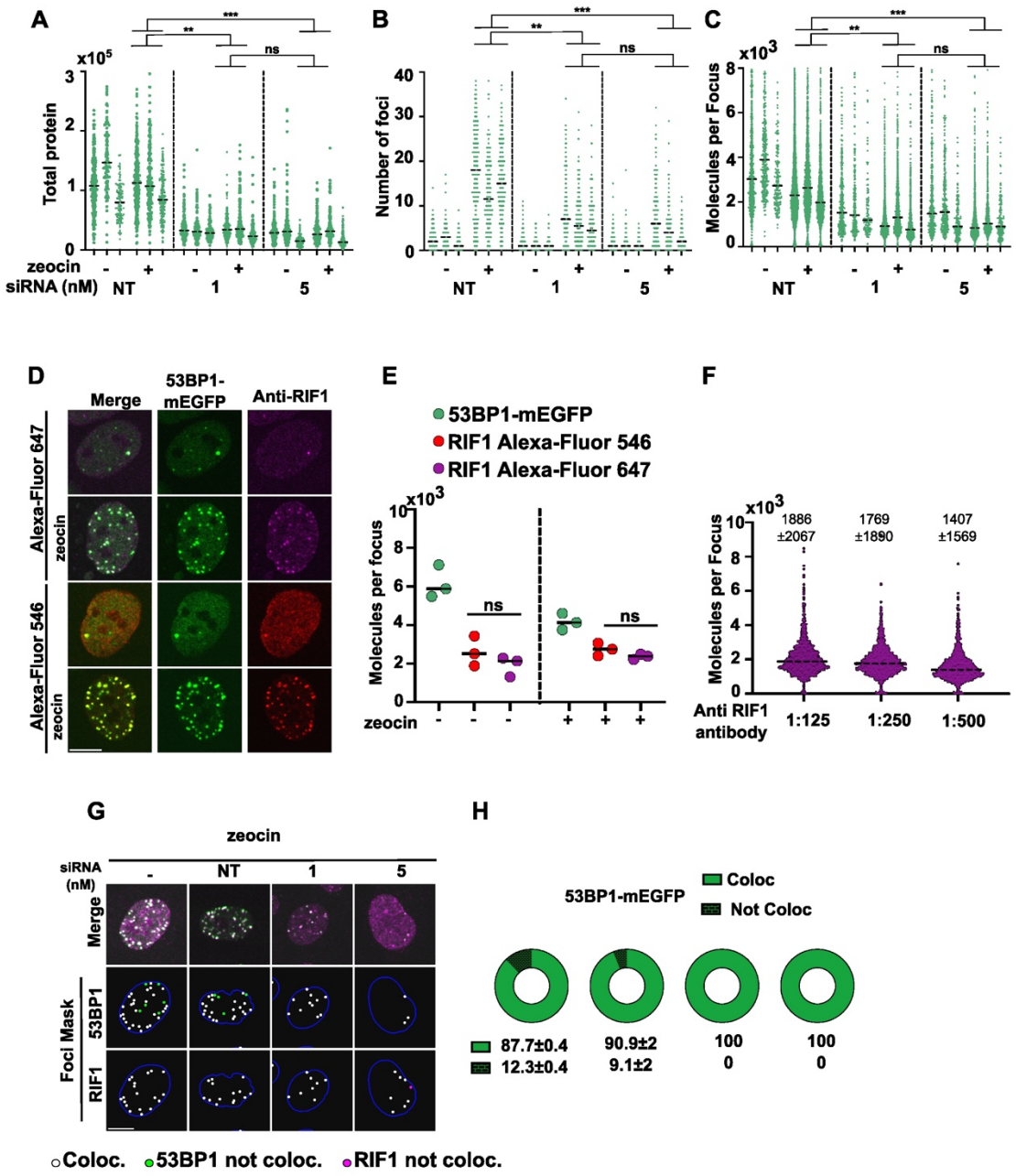

Fig. S4. (A-C) 53BP1 down regulation in 53BP1-mEGFP$^{+/-}$ clone. Cells were treated or not with the indicated concentration of non-targeting or 53BP1 siRNA. 48 hrs after treatment, cells were challenged with 500 µg/mL of zeocin, fixed, and imaged using a confocal microscope. (A) Total number of 53BP1 molecules in the focal plane, (B) number of 53BP1-mEGFP$^{+/-}$ foci and (C) number of molecules per focus in cells treated or not with siRNA. Data distribution of n=3 replicates, dotted line indicates the mean, n>200 cells per condition, statistical analysis performed on the median. (D) Comparison of RIF1 number of molecules calculated with Alexa-Fluor 647 and Alexa-Fluor 546. 53BP1-mEGFP cells were treated with 500 µg/mL of zeocin, fixed, and immunofluorescence performed with antibody against RIF1. Signal was revealed using a secondary antibody conjugated with Alexa-Fluor 647 or Alexa-Fluor 546 as indicated. (E) Median number of molecules per focus of RIF1 calculated after detection with Alexa-Fluor 546 and Alexa-Fluor 647 of n=3 replicates, n>200 cells per condition in each experiment, statistical analysis performed on the median. (F) Number of molecules per focus in U2OS cells treated with 500 µg/mL of zeocin and calculated using the indicated concentration of anti-RIF1 antibody, median is indicated for each condition. (G) Representative example of foci segmentation and co-localization analysis of cells shown in panel 3A. (H) Pie chart distributions of 53BP1 foci colocalizing or not co-localizing with RIF1. Cells were treated for 1 hour with zeocin at the indicated concentration, followed by medium replacement, and one hour of recovery before fixation. NT, Non-Targeting ns, not significant, **P≤0.01; ***P≤0.001, (A-C) one-way ANOVA with Tukey's post-hoc test; (E-F) unpaired, two-tailed Student t-test. Scale bar 10 µm.

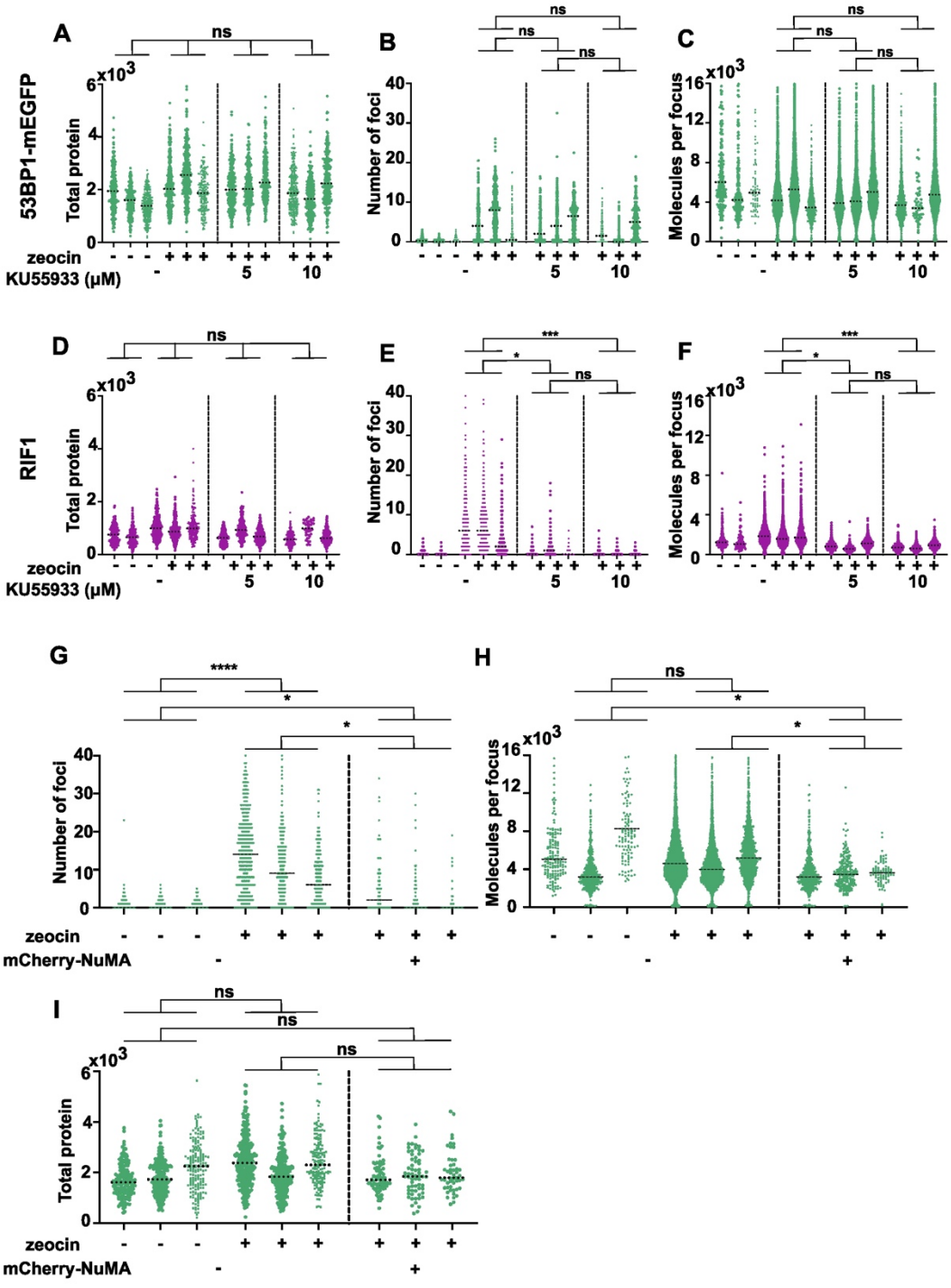

Fig. S5. Individual data point distribution of (A-F) total protein in the focal plane in number of molecules, number of foci per cell, molecules per focus of (A-C) 53BP1-mEGFP and (D-F) RIF1, in cells treated or not with ATM inhibitor KU55933 and zeocin. Data show distribution of n=3 replicates as a complement for the bar plots shown in Figure 4. Dotted line represents the mean. (G-I) Individual data point distribution of number of foci per cell, molecules per focus, and total protein in the focal plane in number of molecules of 53BP1-mEGFP, in cells overexpressing mCherry-NuMA or not, and treated with zeocin as indicated. Data show distribution of n=3 replicates as a complement for the bar plots shown in Figure 5. Dotted lines represent the mean. Statistical analysis was performed on the median. Ns, not significant, *P≤0.05, ***P≤0.001; unpaired, two-tailed Student t-test.

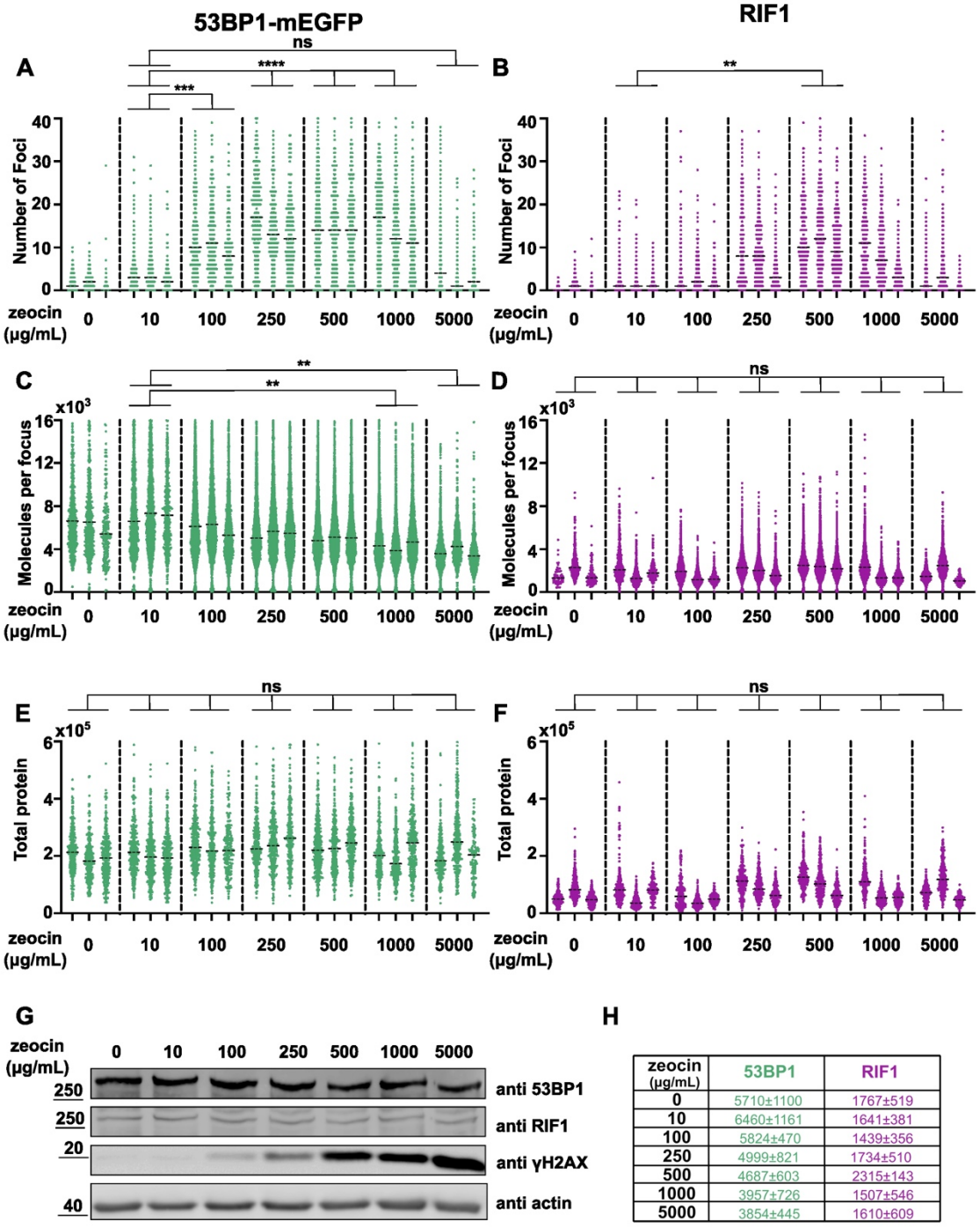

zeocin (μg/mL)	53BP1	RIF1
0	5710±1100	1767±519
10	6460±1161	1641±381
100	5824±470	1439±356
250	4999±821	1734±510
500	4687±603	2315±143
1000	3957±726	1507±546
5000	3854±445	1610±609

Fig. S6. Individual data point distribution of (A-B) number of foci per cell, (C-D) molecules per focus, and (E-F) total protein in the focal plane in number of molecules, of respectively 53BP1-mEGFP and RIF1 in cells treated with the indicated zeocin concentrations. Data show distribution of n=3 replicates as a complement for the bar plots shown in Figure 6. Dotted line represents the mean. (G) Immunoblotting validation of protein level upon zeocin challenge. Lysates from cells with the indicated doses of zeocin were loaded on a 6% or 12% SDS-PAGE and blotted with anti-53BP1, anti-RIF, anti-γH2AX or anti-actin antibodies. (H) Average number of molecules per focus calculated for 53BP1-mEGFP and RIF1 at indicated zeocin concentration. Statistical analysis was performed on the median. ns, not significant, **P≤0.01; ***P≤0.001, ****P≤0.0001, one-way ANOVA with Tukey's post-hoc test.

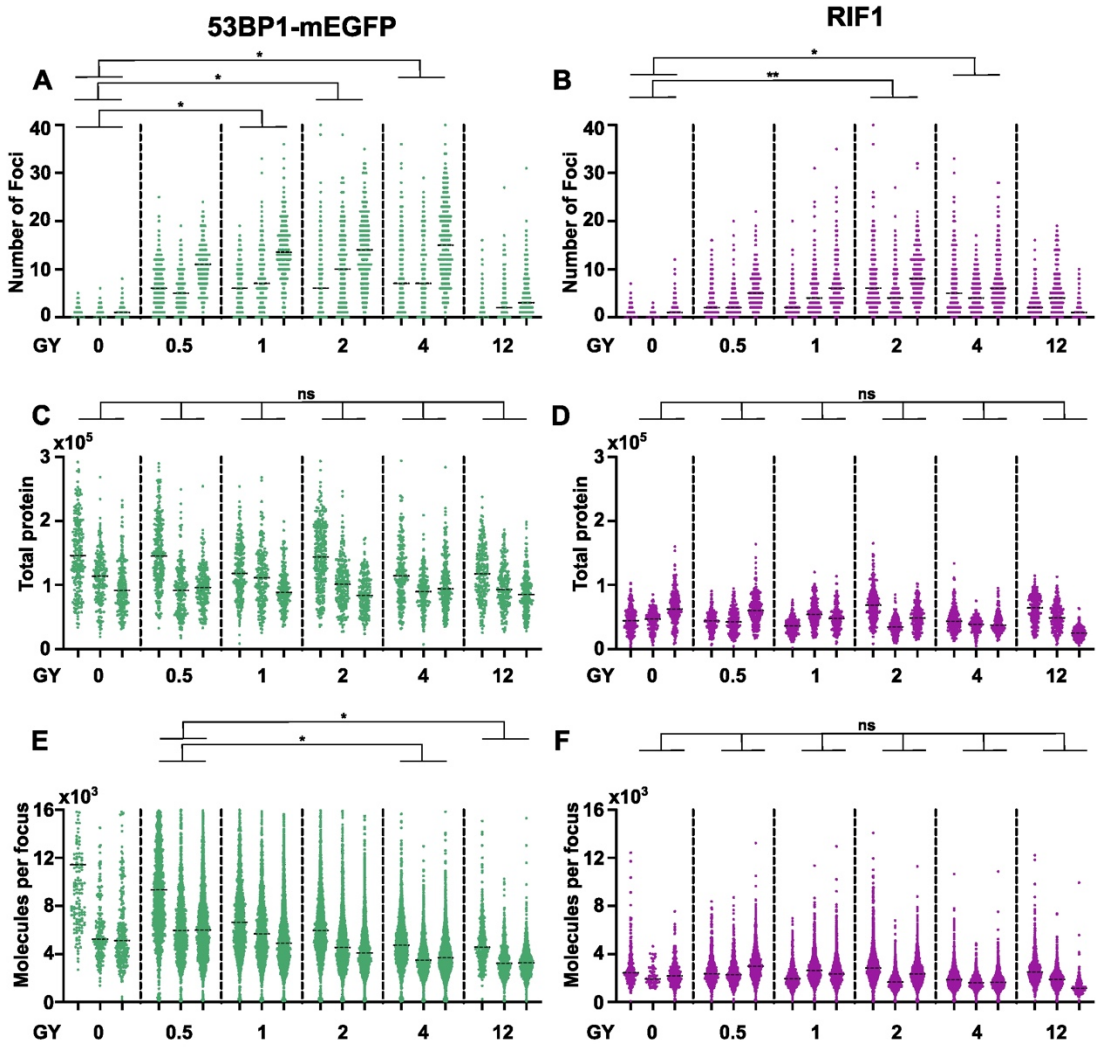

G

GY	53BP1	RIF1
0	7257±3615	2183±254
0.5	7100±1947	2537±388
1	5734±872	2300±340
2	4868±971	2284±584
4	3972±669	1705±133
12	3687±761	1846±681

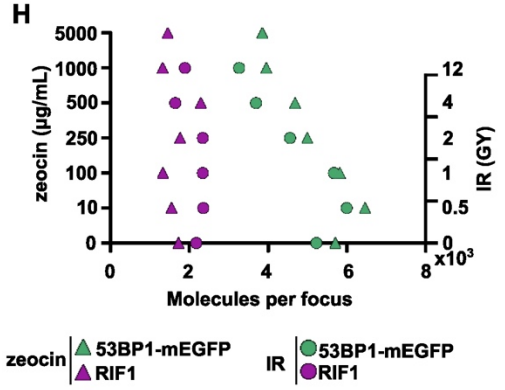

Fig. S7. Individual data point distribution of (A-B) number of foci per cell, (C-D) total protein in the focal plane in number of molecules, and (E-F) molecules per focus, of respectively 53BP1-mEGFP and RIF1 in cells treated with the indicated IR doses. Data shows the distribution of three replicates as a complement for the bar plots shown in Fig. 7. Dotted line represents the mean. (G) Average number of molecules per focus calculated for 53BP1-mEGFP and RIF1 at indicated GY dose. (H) Comparison of changes in molecules per focus of 53BP1-mEGFP and RIF1 upon exposure to IR (triangles) or zeocin (circles). Statistical analysis was performed on median. *P≤0.05; **P≤0.01, one-way ANOVA with Tukey's post-hoc test.

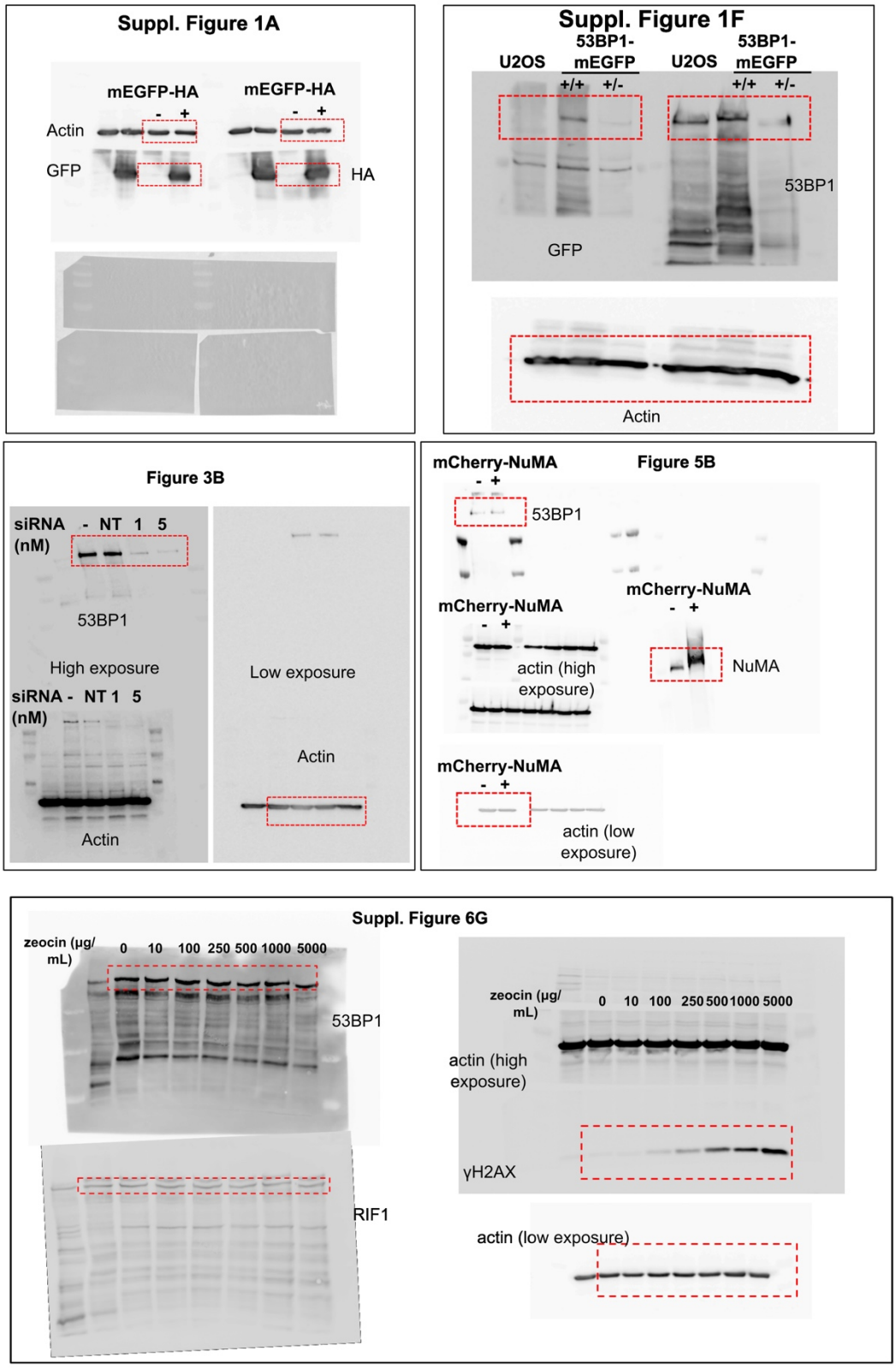

Fig. S8. Blot transparency